JOURNAL OF GEOPHYSICAL RESEARCH, VOL. 115, D12119, doi:10.1029/2009JD013241, 2010

Three-dimensional charge structure of a mountain thunderstorm

William W. Hager,[1] Beyza Caliskan Aslan,[2] Richard G. Sonnenfeld,[3] Timothy D. Crum,[4] John D. Battles,[5] Michael T. Holborn,[6] and Ruth Ron[6]

Received 23 September 2009; revised 1 December 2009; accepted 20 January 2010; published 23 June 2010.

[1] Lightning charge transport is analyzed for a thunderstorm which occurred on 18 August 2004 near Langmuir Laboratory in New Mexico. The analysis employs wide band measurements of the electric field by a balloon-borne electric field sonde or Esonde, simultaneous Lightning Mapping Array measurements of VHF pulses emitted during lightning breakdown, and Next Generation Weather Radar data. The thunderstorm was composed of two principal updrafts. In the stronger updraft the positively charged particles reached altitudes up to 14 km, and in the weaker updraft the positive particles reached 11 km altitude. The negatively charged particles generated in the updraft appeared to reach altitudes up to 10 km in the strong updraft and 8 km in the weaker updraft. Just outside the updrafts the positive and negative particles drop sharply; thereafter, they drop down at a nearly linear rate, between 1 and 2 km in altitude per 10 km in horizontal distance. Initially, as the updraft developed, most charge was transported by updraft flashes; later, after about 15 to 20 min, extensive flashes were predominant. Most cloud-to-ground (CG) flashes transported negative charge from outside the updraft at 6 km altitude down to ground; however, some strokes of a CG reached into a higher negative charge region closer to the updraft. Nearly 6 times as much charge was transported by intracloud (IC) flashes when compared to CG flashes. The ratio of the average charge transport for an IC flash to the average charge transport for a CG flash was 1.6, while the average generator current associated with the combined updrafts was 2.3 amperes for 40 min.

Citation: Hager, W. W., B. C. Aslan, R. G. Sonnenfeld, T. D. Crum, J. D. Battles, M. T. Holborn, and R. Ron (2010), Three-dimensional charge structure of a mountain thunderstorm, *J. Geophys. Res.*, *115*, D12119, doi:10.1029/2009JD013241.

1. Introduction

[2] *Sonnenfeld et al.* [2006] describe a newly developed balloon-borne electric field sonde or Esonde which can be used to measure thundercloud electric field changes. *Hager et al.* [2007] develop new techniques for analyzing lightning-associated charge transport in a thundercloud by using data from the Esonde and simultaneous Lightning Mapping Array (LMA) measurements of VHF pulses emitted during lightning breakdown processes. See *Coleman et al.* [2003], *Rison et al.* [1999], and *Thomas et al.* [2001, 2004] for a description of the New Mexico Institute of Mining and Technology LMA network. *Hager et al.* [2007] analyzed one cloud-to-ground (CG) and two intracloud (IC) flashes observed on 18 August 2004 near Langmuir Laboratory.

[3] The focus in this earlier work was on the movement of charge along the lightning channel as a function of time. In this paper, our goal is to understand what we can of the whole storm charging and discharging process. We have three tools for this task, pulse data from the LMA, electric field data from the Esonde, and products from the National Climatic Data Center (NCDC) in conjunction with Plan Position Indicator (PPI) scans from the Albuquerque Next Generation Weather Radar (NEXRAD)(also known as Weather Surveillance Radar-1988, Doppler, or WSR-88D). The LMA pulse data tend to outline regions of positive and negative charge. Using the LMA channel source points together with Esonde data, we reduce CG strokes and IC flashes to equivalent monopoles and dipoles. The convective cores seen in the NEXRAD data correlate nicely with the Esonde and LMA analysis. Herein, we analyze the total charge transport for nine CG flashes, composed of 44 strokes, and 15 IC flashes, out of the 41 CG and 149 IC flashes within 15 km of the balloon. Our goal is to develop an understanding of the regions in the thunderstorm where charge is transported.

[1]Department of Mathematics, University of Florida, Gainesville, Florida, USA.
[2]Department of Mathematics and Statistics, University of North Florida, Jacksonville, Florida, USA.
[3]Department of Physics and Langmuir Laboratory, New Mexico Institute of Mining and Technology, Socorro, New Mexico, USA.
[4]WSR-88D Radar Operations Center, NWS, NOAA, Norman, Oklahoma, USA.
[5]Space Instrumentation and Systems Engineering, Los Alamos National Laboratory, Los Alamos, New Mexico, USA.
[6]School of Architecture, University of Florida, Gainesville, Florida, USA.

0148-0227/10/2009JD013241

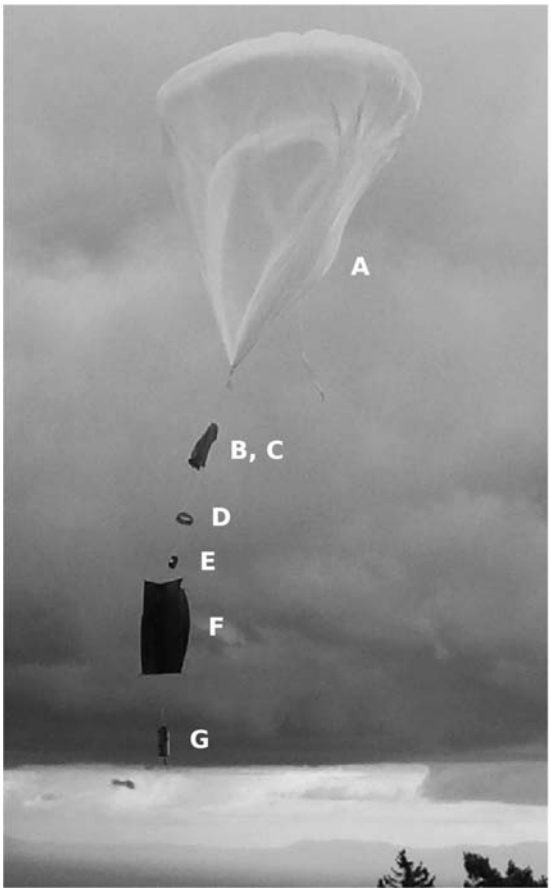

Figure 1. Balloon train including polyethylene balloon (A), 1.6 m diameter nylon parachute (B), balloon cutdown package hidden inside parachute (C), antitangle ring (D), auxiliary tracking package (E), nylon damper (F), and Esonde (G).

[4] In papers connected with the Severe Thunderstorm Electrification and Precipitation Study (STEPS) and with the Thunderstorm Electrification and Lightning Experiment (TELEX), charge structures are inferred in complex multicell thunderstorms, supercells, and inverted polarity storms utilizing LMA data and electric field measurements [e.g., see *Bruning et al.*, 2007; *Rust et al.*, 2005; *Tessendorf et al.*, 2007; *Wiens et al.*, 2005; *Weiss et al.*, 2008]. In this paper, our focus is on a normal polarity mountain storm and the charge structure around a strong updraft which develops, reaches maturity, and dissipates during the flight of the Esonde. Also, the analytical techniques from the previous paper [*Hager et al.*, 2007] are further enhanced to take better account of instrument rotation and to compute the horizontal electric field. The previous techniques worked well when the instrument experienced slow, steady rotation, while the new technique developed in this paper can be used to compute the electric field when the instrument rotates more rapidly.

[5] The paper is organized as follows: section 2 gives an overview of the balloon flight, while section 3 discusses the structure of the thunderstorm. The methods used to determine the electric fields and charge transport are summarized in section 4. Section 5 analyzes several noteworthy flashes. Section 6 presents the charge transport analysis for all the flashes in our study, followed by the conclusions in section 7.

1.1. Dipole Sign Convention

[6] Throughout the paper we will be referring to the location of charge centers. Beginning with Figure 18, either a box or a solid colored circle represents a region from which negative charge has been removed, while either an asterisk or a plus enclosed in a circle represents a region where positive charge was neutralized. We refer to the box (or solid circle) as the "dipole center in region of negative cloud charge" and the asterisk (or circled plus) as the "dipole center in the region of positive cloud charge." This language is employed since we are trying to use the calculated dipole signs to draw conclusions about the sign of the local cloud charge. The regions of negative and positive cloud charge correspond to the positive and negative ends, respectively, of the dipole which fits our measurements.

1.2. Polarity Convention

[7] The sign convention we employ for the electric field is that it points away from a positive charge. Equivalently, the direction of the electric field is the direction of the force that would be exerted on a positive test charge.

1.3. Coordinate System

[8] Throughout the paper, the coordinates in plots are relative to an origin at sea level directly below a point near the NW corner of the annex building of Langmuir Laboratory. The positive x axis is directed to the east, the positive y axis points to (true) north, and the z axis is vertical, pointing away from the surface of the Earth.

1.4. N3R Radar Scan

[9] Throughout the paper, we make reference to N3R radar scans. The label "N3R" is the NEXRAD naming convention for data files associated with radar scans whose angles of tilt are nominally 3.35°.

2. Overview of the Balloon Flight

[10] On 18 August 2004, at approximately 1948:30 UT, the balloon-borne Esonde was launched from the balloon hanger at Langmuir Laboratory (latitude 33.97528°N, longitude 107.18072°W, and altitude 3255 m) in the Magdalena Mountains of New Mexico, near New Mexico Institute of Mining and Technology. A photo of the balloon flight package appears in Figure 1. The balloon ascended to about 4290 m, dropped to about 2510 m, and ascended again to 3650 m (see Figure 2). The balloon descent was probably due to the accumulation of ice. As the balloon descended to lower altitudes, the ice melted and fell from the balloon, allowing the subsequent ascent. When the cutdown package was activated, the balloon was detached from the Esonde, and the instrument, with data stored in flash memory, dropped into a flat plain 26.6 km southeast of Langmuir Laboratory at latitude 33.7723°N, longitude 107.0493°W, and elevation 1570 m. The flight lasted about 61.5 min and a thunderstorm was active within 15 km of the balloon during the first 45 min of the flight.

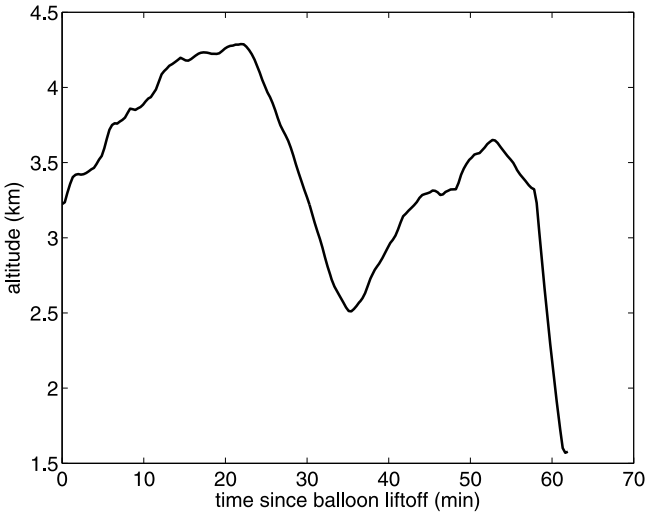

Figure 2. Balloon altitude as a function of time since launch at 1948:30 on 18 August 2004.

[11] Figure 3 is a Google Maps satellite view of the area around Langmuir Laboratory along with the superimposed balloon trajectory. The Rio Grande is the green ribbon in Figure 3; the balloon flies southeast of Langmuir Laboratory after it is launched near the summit of South Baldy Peak. We studied the thunderstorm as it passed through a region which extended roughly 40 km north/south and 30 km east/west. This region was close enough to the Esonde that we were able to analyze charge transport from lightning. Our analysis will show that there are two primary updrafts. In Figure 3, we label these U1, a strong updraft with LMA pulses reaching 14 km altitude, and U2, a weaker updraft with LMA pulses reaching 11 km altitude. The cells north and west of the study region, labeled U3 and U4, were the target of some flashes which emanate from the study region.

[12] NEXRAD composite radar images recorded at the National Weather Service station KABX, Albuquerque (latitude 35.1497°N, longitude 106.8233°W, antenna elevation 1814 m) are given in Figure 4. For an overview of NEXRAD capabilities, see *Crum et al.* [1993], *Crum and*

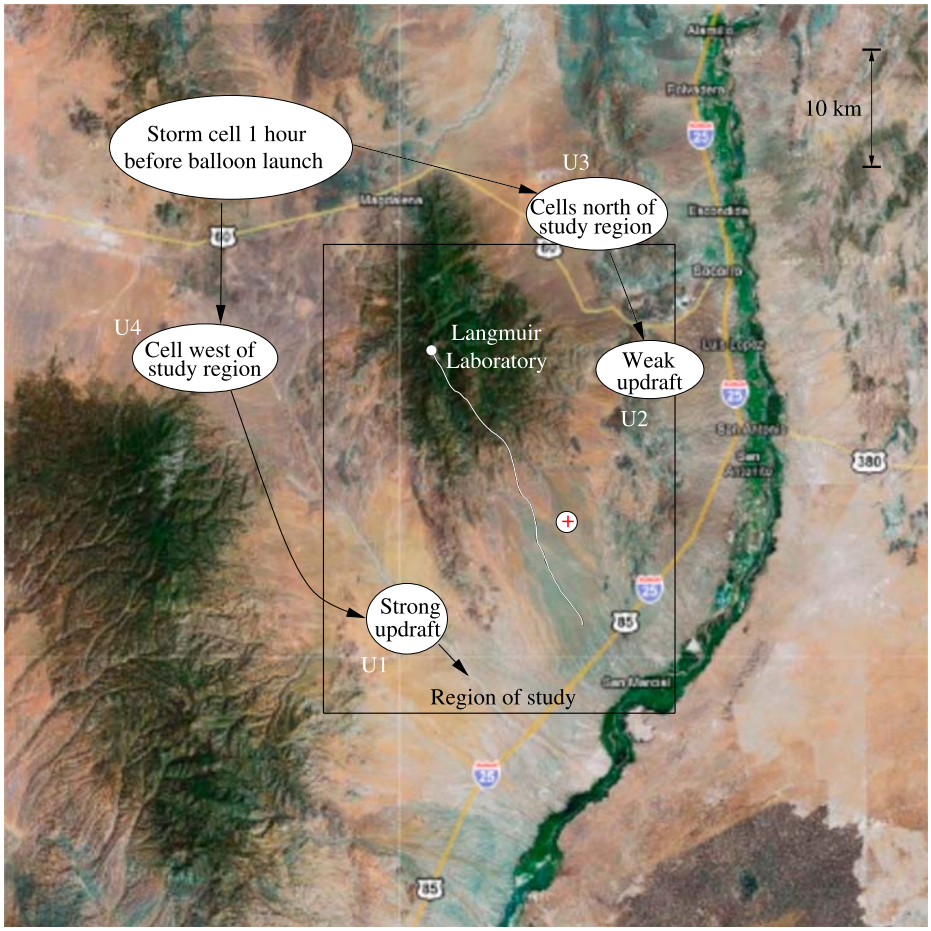

Figure 3. A Google Maps satellite view of the area around Langmuir Laboratory. About 1 h before balloon launch on 18 August 2004 the storm activity is located about 20 km northwest of Langmuir Laboratory. The storm wraps around South Baldy Peak and Langmuir Laboratory as it travels southeast. The balloon-borne Esonde launched from near Langmuir Laboratory is carried by the wind southeast along the flight path shown in white. The principal updrafts in the region of study are labeled U1 and U2. The cells north and west of the study region, labeled U3 and U4, are the target of some flashes emanating from the study region. The region in the storm where positive charge was neutralized by an IC flash, denoted Flash 2, is indicated by a plus in a white circle, while the origin of the flash is colocated with U1.

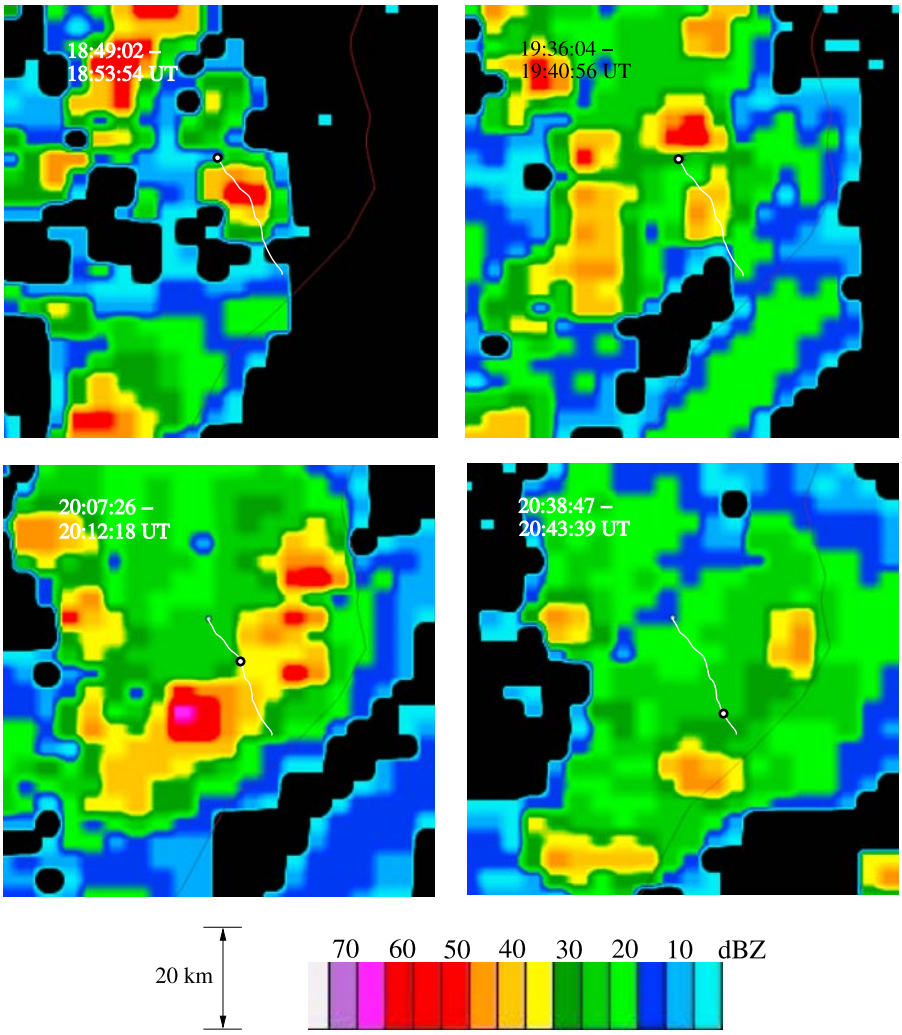

Figure 4. PPI composite reflectivity product from the National Weather Service KABX NEXRAD (Albuquerque, New Mexico), showing a 90 km by 90 km region. The balloon flight path, shown in white, originates at Langmuir Laboratory (small white circle). On each plot, we give the time of the beginning and end of the volume scan. The location of the balloon at the start of each volume scan is indicated by a black circle. A distance scale and a reflectivity legend are given at the bottom.

Alberty [1993], *Crum et al.* [1998], and *Klazura and Imy* [1993]. The trajectory of the balloon is superimposed on the radar image, with the balloon location at the time of the radar image circled in black. The balloon-borne Esonde was launched from Langmuir Laboratory on the northwest end of the trajectory. One hour before the balloon launch, at 1849 UT, the thunderstorm that we study appears as a line of storm activity about 20 km northwest of Langmuir Laboratory. The 1936 UT radar image of Figure 4 reflects a point in time about 12 min before launch. The 2007 UT radar image of Figure 4 is during the peak thunderstorm activity. The strongest reflectivities, southwest and east of Langmuir Laboratory, correspond to the "strong updraft" U1 and "weak updraft" U2 in Figure 3. By the time of the 2038 UT radar image, the strength of the storm is diminished. An animated gif showing the radar images from 1843 UT up to 2044 UT is available in the auxiliary material (Animation S1).[1]

3. Storm Structure

[13] The thunderstorm updrafts play a key role in the development of the thunderstorm charge structure. Positive and negative charge are generated in updrafts and propelled vertically; the prevailing wind then displaces the charged particles horizontally. In this paper, we express the charge structure of the storm relative to the location of the updrafts which are determined in this section. Since we do not have wind velocity measurements for the storm, we infer the location of the updrafts using both LMA data and radar images.

[1]Auxiliary material data sets are available at ftp://ftp.agu.org/apend/jd/2009jd013241. Other auxiliary material files are in the HTML.

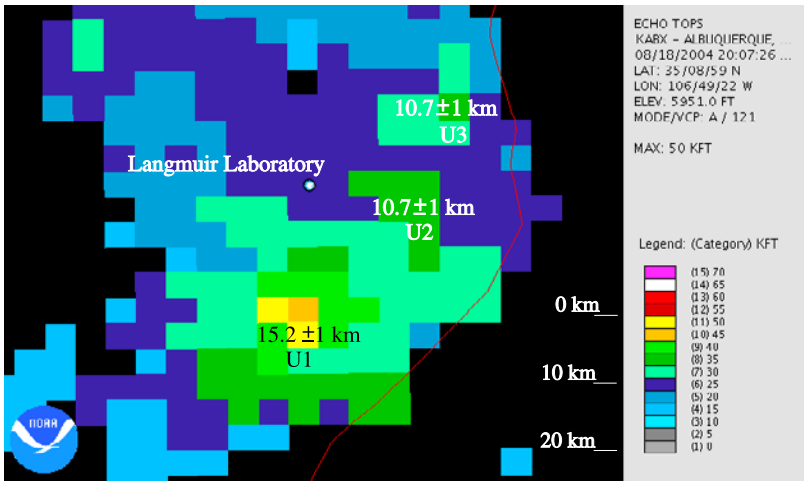

Figure 5. Echo tops seen by the KABX NEXRAD for the region surrounding Langmuir Laboratory (the white dot) between 2007:26 UT and 2012:18 UT. The altitudes of the echo tops near updrafts U1, U2, and U3 are indicated.

[14] *Lhermitte and Krehbiel* [1979] report that for a thunderstorm studied during the 1978 Thunderstorm Research International Program (TRIP) at the Kennedy Space Center, reflectivity values in excess of 50 dB*Z* were observed within the vicinity of the updraft. These relatively high values for the reflectivity were attributed to graupel or hail that was suspended in the updraft and which grew by riming of supercooled water droplets. The 65 dB*Z* purple region in Figure 4 (bottom left) is a clear candidate for an updraft location.

[15] The NEXRAD Echo Tops product for 2007 UT, near the peak of storm intensity, is shown in Figure 5. This product measures the altitude of highest reflectivity exceeding 18.5 dB*Z* for each 4 km by 4 km grid box above the surface of the Earth. The highest echo tops correspond to the three updrafts labeled U1, U2, and U3 in Figure 3. As indicated in Figure 5, the highest echo tops are 15.2 ± 1 km near U1 and 10.7 ± 1 km near U2 and U3.

[16] The rising air in an updraft of a mountain storm transports hydrometeors vertically to a higher altitude than that of hydrometeors outside the updraft. A radar beam that passes through the top of a thunderstorm indicates a reflectivity peak in an updraft and becomes weaker outside the updraft. The location of the updrafts are not seen clearly in the composite radar images of Figure 4 since hail, graupel, or rain which are outside the updraft can also generate significant reflectivity. The location of the updrafts are clearer in the N3R radar scans shown in Figure 6. As mentioned earlier, the label "N3R" is the NEXRAD naming convention for data files associated with radar scans whose angles of tilt are nominally 3.35°. The width of the beam is approximately 0.93°. These details and others related to N3R can be found in the Federal Meteorological Handbook 11, Doppler Radar Meteorological Observations, 2006, Part C, Table 5-4 and Part D, paragraph 2.2.1. The handbook is available at http://www.ofcm.gov/homepage/text/pubs.htm.

[17] In the vicinity of U1, N3R scans from 11.7 km up to 14.3 km altitude (from the bottom to the top of the main beam); in the vicinity of U2, N3R scans from 9.9 km up to 12.1 km altitude. These radar elevations roughly match the highest echo tops labeled in Figure 5. Hence, N3R radar roughly scans the cloud tops, and the regions of highest reflectivity should correspond to the location of the updrafts.

[18] Figure 6 shows four N3R radar plots. The first scan is about 15 min before balloon launch, and the last is near the peak of storm activity. The three reflectivity cores clearly visible in the last scans are identified with U1, U2, and U3 in Figure 3. U2 was first clearly visible in the N3R scans made between 2004:49 UT and 2005:35 UT (not shown). U1 appears to be much stronger than U2 since the reflectivity is much larger; also, we will see that the LMA pulses near U1 reach 14 km altitude, while the LMA pulses near U2 approach 11 km altitude.

[19] Looking at the earlier 1933–1934 UT radar scans in Figure 6, we see reflectivity cores about 9 km southeast of Langmuir Laboratory, about 12 km west of Langmuir Laboratory, and just north of Langmuir Laboratory. All of these are diminishing in strength. The latter two reflectivity cores correspond to U3 (cells north of study region) and U4 (cell west of study region) in Figure 3. Notice that in each plot in Figure 6, the reflectivity is higher in the region north of Langmuir Laboratory, when compared to the region south of Langmuir Laboratory. One reason for this difference in reflectivity is that the radar beam is closer to the surface of the earth north of the laboratory; at lower altitudes, the radar begins to penetrate the clouds as well as cloud tops, leading to increased reflectivity. The altitude of the center of the radar beam is given on the concentric circles in Figure 6.

[20] By 1954 UT, about 5 min after launch, we see in Figure 6 that the reflectivity core southeast of Langmuir Laboratory is becoming less intense while the reflectivity core west of the laboratory (U4) is now missing. Instead, a new reflectivity core U1, about 20 km southwest of the laboratory, begins to emerge. The reflectivity at this location continues to intensify in the subsequent radar scans.

[21] An animated gif showing the N3R radar scans between 1949 UT (just after balloon launch) up to 2047 UT is available in the auxiliary material (Animation S2). In Figure 7, we plot the center of the region of largest reflectivity for U1 and U2 as a function of time. The time

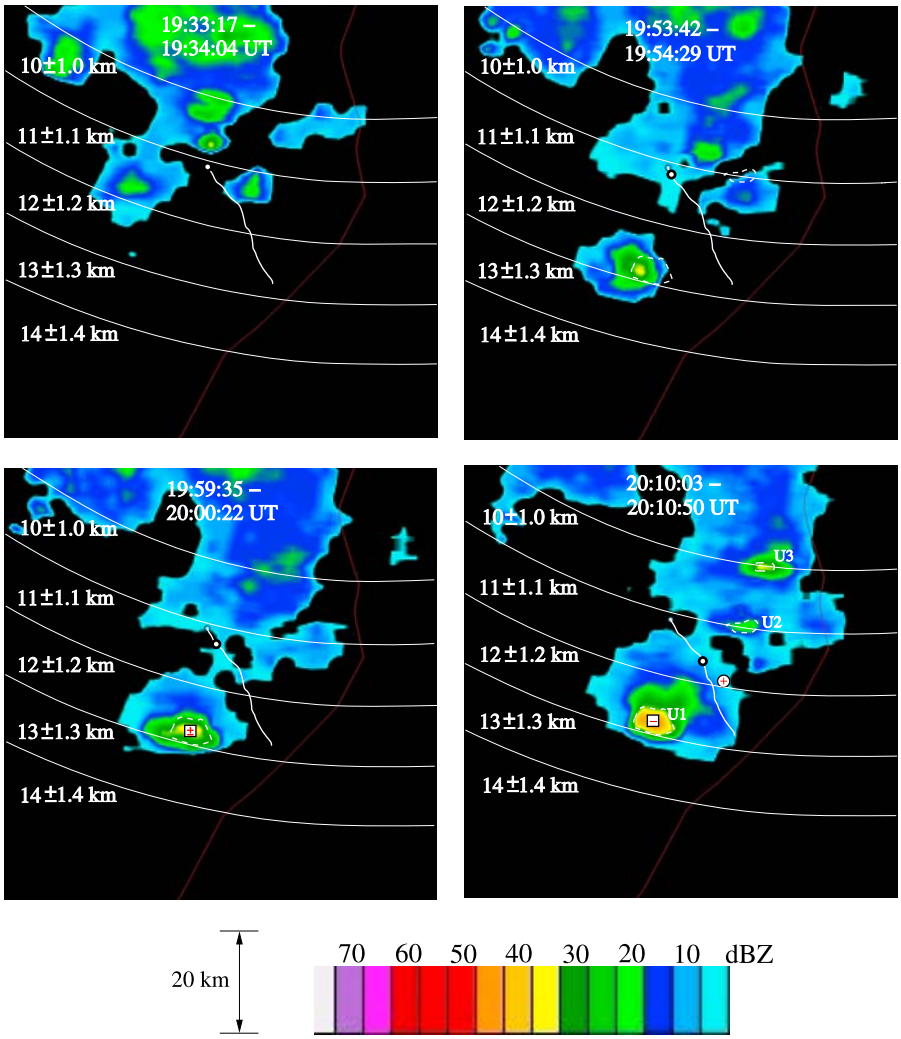

Figure 6. N3R reflectivity from the National Weather Service KABX NEXRAD (Albuquerque, New Mexico), showing a 90 km by 90 km region. The balloon flight path, shown in white, originates at Langmuir Laboratory. The location of the balloon at the time of the radar image is indicated by a black circle. The altitude of the center of the radar beam appears on the circular arcs centered at the KABX NEXRAD. The tolerances correspond to the top and bottom of the beam. A distance scale and reflectivity legend are given at the bottom. The regions of highest reflectivity between 2010:03 UT and 2010:50 UT (dashed white curves) are also shown. We show the dipole charge centers for Flash 1, an updraft flash, which took place about 3 min before the 1959:35–2000:22 UT plot. The dipole charge centers for Flash 2, which took place about 3 min before the 2010:03–2010:50 UT scans, are also shown. The plus and minus correspond to the charge centers in the regions of positive and negative cloud charge, respectively.

between radar scans and hence, the time between successive locations for U1 or U2 in Figure 7, is about 5 min. In Figure 7 (bottom) the black dot is the mean location of U1 between 2000 and 2015 UT. The box is the mean location ±1 km vertically and ±2.7 km horizontally, which corresponds to the radar resolution. In Figure 7 (top) the black dot is the mean location of U2 between 2005 UT and 2026 UT. Observe that both U1 and U2 are relatively stationary. For comparison, the balloon is traveling SSE at about the speed 24 km/h. As U1 begins to disintegrate between 2021 UT and 2026 UT, its velocity and direction of motion begin to approach that of the prevailing wind.

[22] We now show a three-dimensional view of U1 from the NCDC Weather and Climate Toolkit. The ArcScene product in the Toolkit allows us to view layers of level II radar data, stacked above a satellite view of the Earth. In Figure 8, we view the storm from a reference point on the east side of the Rio Grande (the green ribbon in the foreground). The five layers in Figure 8 correspond to scans which start at 2002:12 UT at the tilt angle 0.49°, and end 3 min 58 s later at the tilt angle 4.27°. The black vertical straw corresponds to the mean location of U1 (the black dot) shown in Figure 7. Since the regions of high reflectivity, which correspond to the updraft, follow the straw, the updraft is approximately vertical. The altitude at which the center of the 4.27° radar beam cuts the straw is approximately 15.5 km. The highest LMA pulses near U1 reached an

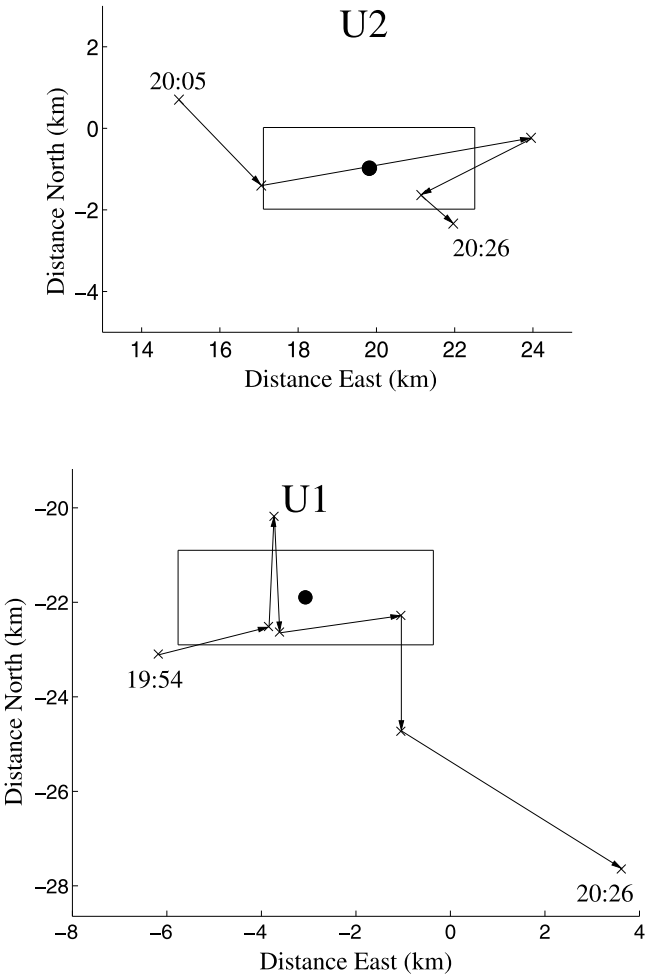

Figure 7. Location of U1 and U2 as a function of time. A cross is placed at the center of the reflectivity core in each radar image; about 5 min separate each cross in the path. (bottom) For U1 the black dot is the mean location between 2000 UT and 2015 UT. (top) For U2 the black dot is the mean location between 2005 UT and 2026 UT. The box surrounding each black dot is obtained by adding and subtracting the resolution of the radar.

altitude between 14 km and 15 km; hence, the highest LMA pulses are very near the highest radar echoes.

[23] LMA data provide a different strategy for inferring the location of updrafts. The locations we obtain confirm the locations deduced from the radar images. As noted by *Vonnegut* [1983], "it is important to recognize that it is the electric field and not the charged particles that are of dominant importance in causing lightning and determining where it goes." The lightning channel is generated by large electric fields; there may or may not be significant charge near the channel. For example, in the "bolt from the blue," lightning propagates in clear air. On the other hand, it is highly likely that there are charged particles in the regions at the ends of the channel. Since the highest LMA pulses often correspond to the ends of channel segments (see Flashes 1 through 5, sections 5.1–5.5), the highest LMA pulses indicate the location of some charged particles in the cloud.

[24] Let us consider the time interval between 2002 UT and 2012 UT when the thunderstorm was quite active. In Figure 9, we plot the location in the *xy* plane of all LMA pulses with altitude at least 13 km in the lower left corner and with altitude at least 10 km in the upper right corner. The contours of high reflectivity delineated in Figure 6 correspond to the solid curves in Figure 9. Comparing Figures 6 and 9, we see that the regions of high N3R reflectivity are approximately regions where the relatively highest LMA pulses were detected. The resolution of the radar images is 1° azimuthal and 1 km in range, as indicated on page 1677 of *Crum et al.* [1993]. This works out to about 2.7 km in the east/west direction and 1 km in the north/south direction at the location of U1. Hence, the reflectivity cores in Figure 6 at 2010 UT agree to within the radar resolution with the location of the high LMA pulses. The N3R image implies that there are elevated particles in these regions of high reflectivity. The LMA data indicate there are charged particles in these regions which are more elevated than the surrounding charged particles. Together, the LMA and radar data imply that updrafts are located at U1 and U2, the two principal generators of charge in the region of study.

[25] Notice that there is an arc of high LMA pulses south of U2 in Figure 9. Since the balloon trajectory shows the direction of the prevailing wind, these high LMA pulses are downwind from U2. These downwind LMA pulses could possibly have been associated with lightning which propagated into a region containing charged particles that were produced in the updraft and then advected by the wind. As we will see in section 5, a region of high LMA pulses also appears downwind from U1.

[26] In Figure 10, we give a side view of all the LMA pulses associated with the 24 flashes that we analyzed. The first flash occurred at 1956:49 UT, while the last occurred at 2029:06 UT. Hence, the duration between the first and the last flash is about 32 min. Each flash that we analyzed was partitioned into negative and positive parts: the charge transport analysis tells us where charge is moved in a flash, and based on this movement, we associated either a plus or minus sign with each LMA pulse. An example showing how we associated charge sign with the LMA pulses appears in Figure 18. In Figure 10, we color the LMA pulses red in regions where the cloud charge is positive and blue in the regions where the cloud charge is negative. The virtual camera in Figure 10 is located northwest of Langmuir Laboratory, pointing toward the southeast from an altitude of 5200 m. At the location of U1, we see positively charged particles transported much higher than the surrounding particles. The negatively charged particles drop in altitude, almost linearly, as we move away from U1. They increase in altitude as we approach U2. An animated tour of the LMA pulses for the 24 flashes we have analyzed is available in the auxiliary material (Animation S3 and Figures S2–S5).

4. Methodology

[27] In this section we discuss the Esonde and the methods used to recover the electric field and the charge transport due to a flash. The Esonde surface is partially covered by four metallic plates or electrodes. We use the induced charge on each electrode along with the measured rotation of the Esonde to determine the local electric field. The circuits are

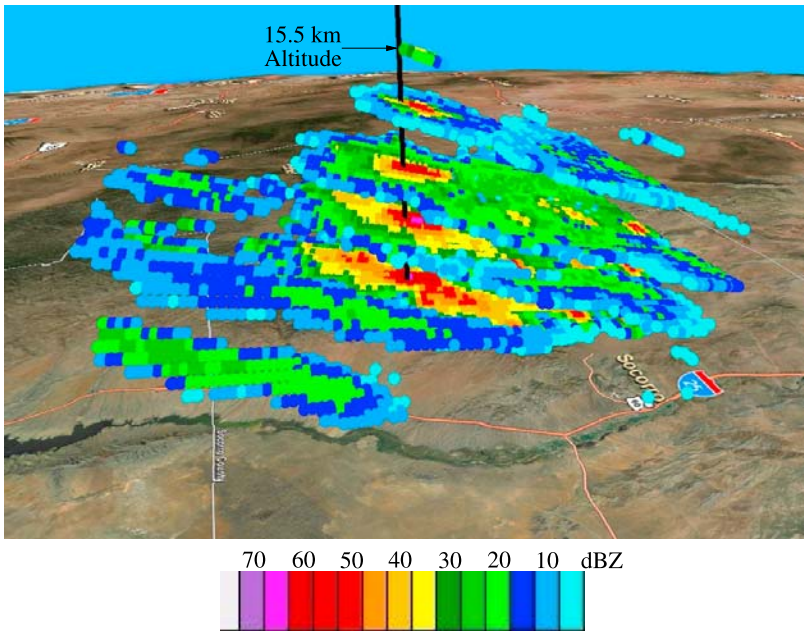

Figure 8. The KABX NEXRAD reflectivity at five angles of tilt, from 0.49° up to 4.27°, arranged in a stack. The volume scan starts at 2002:12 UT at the lowest angle of tilt and ends 3 min 58 s later at the highest angle shown. This view was derived using the NCDC Weather and Climate Toolkit and exported to point data shapes files for display in ESRI ArcScene software. The radar imagery is courtesy of NCDC. The cylindrical volume elements in the plot are 1 km long. The storm is on the western side of the Rio Grande (foreground). The black vertical straw is positioned at the mean location of U1, the black dot in Figure 7 (bottom).

designed to measure the electric field in the frequency band from 1 Hz to 5000 Hz. Data are sampled 10,000 times a second and recorded with 16-bit resolution. Two different techniques were developed for transforming the measured quantities into the local electric field. One technique can be used to compute the electric field change at the Esonde when the instrument experiences slow, steady rotation. The other technique can be used to compute the vertical electric field change and the horizontal electric field when instrument rotation is on the order of 30 or more degrees per second. We begin by summarizing the technique for computing the electric field change, which was developed by *Hager et al.* [2007].

4.1. Recovery of Electric Field Change

[28] The induced charge on any of the four sensing electrodes of the Esonde is transformed into a corresponding voltage by a charge amplifier with a feedback capacitor and resistor. If $V_i(t)$, i = 1, 2, 3, or 4, is the amplifier voltage output associated with electrode i at time t, then the equation relating the electric field $\mathbf{E}$ to the voltage $\mathbf{V}$ is

$$\mathbf{E}(t) - \mathbf{R}(t)\mathbf{R}(0)^{\mathsf{T}}\mathbf{E}(0) = \mathbf{R}(t)\mathbf{M}\mathbf{f}(t), \tag{1}$$

where

$$\mathbf{f}(t) = C\left[\mathbf{V}(t) + \frac{1}{RC}\int_0^t \mathbf{V}(s)ds\right] - C\mathbf{V}(0).$$

Here R and C are the resistance and capacitance of the circuit, $\mathbf{R}(t)$ is a known rotation matrix, and M is a 3 by 4 matrix of sensor gains. Let $\mathbf{E}_m$ denote the (measured) right side of (1),

$$\mathbf{E}_m(t) = \mathbf{R}(t)\mathbf{M}\mathbf{f}(t). \tag{2}$$

Notice that $\mathbf{f}$ and hence $\mathbf{E}_m$ depend on the time origin, which is taken to be $t = 0$.

[29] The electric field $\mathbf{E}$ is the sum of an abrupt electric field change $\mathbf{E}_L$ due to lightning charge transport, and a slowly varying component $\mathbf{E}_p$ associated with the creation and movement of charged cloud particles under the influence of forces such as wind, gravity and the electric field itself,

$$\mathbf{E} = \mathbf{E}_L + \mathbf{E}_p. \tag{3}$$

Let us define the "background" field $\mathbf{E}_b$ by

$$\mathbf{E}_b = \mathbf{E}_p - \mathbf{R}(t)\mathbf{R}(0)^{\mathsf{T}}\mathbf{E}(0). \tag{4}$$

The substitutions (3) and (4) in (1) give

$$\mathbf{E}_L(t) + \mathbf{E}_b(t) = \mathbf{E}_m(t). \tag{5}$$

Thus the measured field $\mathbf{E}_m$ is the sum of an electric field change $\mathbf{E}_L$ due to lightning and a background field $\mathbf{E}_b$. The goal is to separate the lightning field change from the superimposed background field.

[30] If the rotation matrix $\mathbf{R}$ is either small or slowly varying, then the background field is slowly varying, allowing it to be approximated by a low-degree polynomial. The computation of $\mathbf{E}_L$ proceeds as follows: We first select a

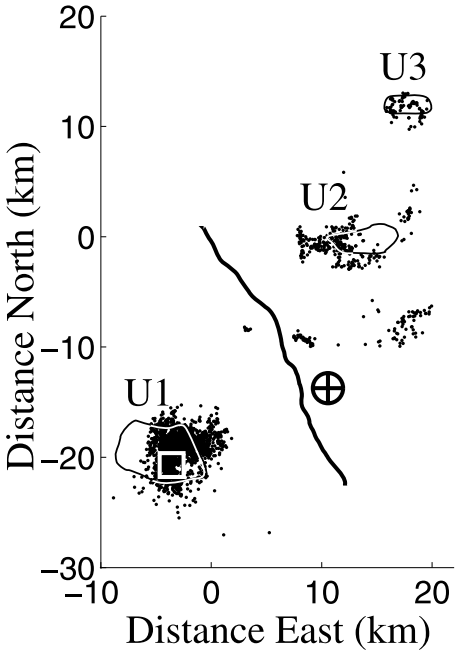

Figure 9. High LMA pulses during the time interval 2002 UT to 2012 UT, a time period when the thunderstorm was very active electrically. The southwest corner shows LMA pulses with an altitude at least 13 km. The northeast corner shows LMA pulses with an altitude at least 10 km. The balloon flight path is plotted near the middle. The locations of the dipole charge centers for Flash 2 (section 5) are indicated by a square (charge center in region of negative cloud charge) and a circle (charge center in region of positive cloud charge). The contours around areas of high reflectivity in the 2010:03–2010:50 UT image of Figure 6 are superimposed. Since the radar resolution is about 2.7 km in the east/west direction and 1 km in the north/south direction, the regions of high N3R reflectivity and relatively high LMA pulses essentially coincide to within the resolution of the radar.

time interval $[p_0, l_0]$ which precedes the stroke, and an interval $[l_1, p_1]$ which follows the stroke. The lightning occurs on the interval $[l_0, l_1]$. During the prestroke time interval $[p_0, l_0]$, we have $\mathbf{E}_L = 0$ and $\mathbf{E}_b(t) = \mathbf{E}_m(t)$. During the poststroke interval $[l_1, p_1]$, $\mathbf{E}_L$ is constant and $\mathbf{E}_b(t) = \mathbf{E}_m(t) - \mathbf{E}_L$. Hence, $\mathbf{E}_b$ after the stroke differs from $\mathbf{E}_m$ by the constant $\mathbf{E}_L$ associated with the lightning charge transport. We fit $\mathbf{E}_b$ before and after the stroke using low-degree polynomials and we choose the constant $\mathbf{E}_L$ after the stroke so that the forward extension of the prestroke background $\mathbf{E}_b$ matches the poststroke background $\mathbf{E}_b$. To illustrate the process, Figure 11 shows the three components of $\mathbf{E}_m$ for an IC which occurred near Langmuir Laboratory on 18 August 2004, shortly after 1956 UT. A detailed study of this flash is given by *Hager et al.* [2007]. In Figure 12, we show the x component of the background field $\mathbf{E}_b$. As can be seen, $\mathbf{E}_b = \mathbf{E}_m$ on the interval $[p_0, l_0]$, while $\mathbf{E}_b$ differs from $\mathbf{E}_m$ on the interval $[l_1, p_1]$ by a constant. On the lightning interval $[l_0, l_1]$, $\mathbf{E}_b$ is estimated by polynomial interpolation. In Figure 13, we show the x component of the lightning electric field, which is obtained from

$$\mathbf{E}_L(t) = \mathbf{E}_m(t) - \mathbf{E}_b(t).$$

4.2. Recovery of the Horizontal Electric Field

[31] When the rotation of the Esonde is large enough, the assumption that $\mathbf{E}_b(t)$ in (4) is a slowly varying function of t is no longer valid. We now describe a different technique for computing $\mathbf{E}_L$, which can be applied when the instrument is rotating more rapidly. This new technique yields the horizontal electric field and the vertical electric field change.

[32] The fundamental assumption for the new technique is that the general behavior of $\mathbf{E}_p$ is known. For the analysis in this paper, we assume that $\mathbf{E}_p$ is approximately a linear function of t during a flash. In other words, $\mathbf{E}_p$ has the form

$$\mathbf{E}_p(t) = \mathbf{c}_0 + \mathbf{c}_1 t, \tag{6}$$

where $\mathbf{c}_0$ and $\mathbf{c}_1$ are vectors with three components. Combining (1), (2), (3), and (6) gives

$$\mathbf{c}_0 + \mathbf{c}_1 t + \mathbf{E}_L(t) - \mathbf{R}(t)\mathbf{R}(0)^{\mathsf{T}}\mathbf{c}_0 = \mathbf{E}_m(t). \tag{7}$$

We evaluate (7) at each sampling time t in both the prestroke interval $[p_0, l_0]$ and the poststroke interval $[l_1, p_1]$. On the prestroke interval, $\mathbf{E}_L$ is zero, while on the poststroke interval, $\mathbf{E}_L$ is constant. This yields a large number of

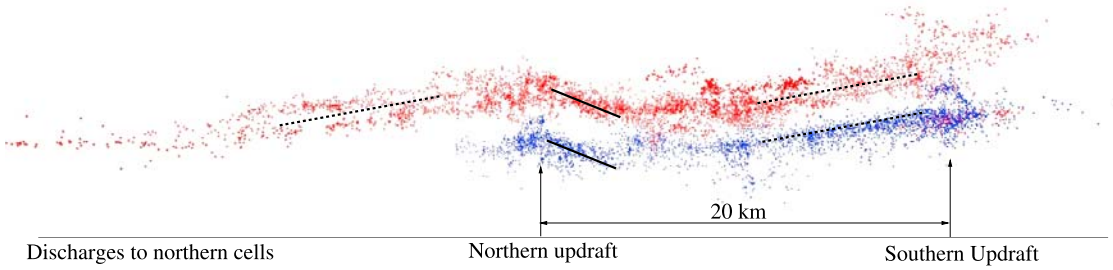

Figure 10. All LMA pulses for the 24 flashes in the study. The view is from northwest of Langmuir Laboratory with a virtual camera pointing southeast from an altitude of 5200 m. In regions of negative cloud charge the LMA pulses are colored blue, while in regions of positive cloud charge the LMA pulses are colored red. Notice the near-linear decay in the average altitude of the pulses. The three dashed line segments on the upwind side of the updrafts and the two solid line segments on the downwind side of the updraft are parallel.

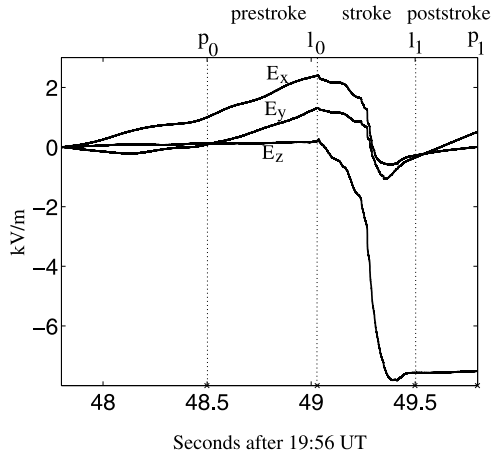

Figure 11. Three components of $\mathbf{E}_m$ for an IC on 18 August 2004, 1956 UT. The flash occurs on the interval $[l_0, l_1]$, while $[p_0, l_0]$ and $[l_1, p_1]$ are prestroke and poststroke intervals used in the analysis.

equations in the following nine unknowns: the three components of the vectors $\mathbf{c}_0$ and $\mathbf{c}_1$, and the postflash $\mathbf{E}_L$. We solve this overdetermined system using least squares. The background field $\mathbf{E}_b$, under the assumption that $\mathbf{E}_p(t)$ is linear, is given by

$$\mathbf{E}_b(t) = \mathbf{c}_0 + \mathbf{c}_1 t - \mathbf{R}(t)\mathbf{R}(0)^{\mathsf{T}}\mathbf{c}_0.$$

Figure 14 plots both $\mathbf{E}_b$ and $\mathbf{E}_m$. Figure 15 shows the x component of $\mathbf{E}_L(t) = \mathbf{E}_m(t) - \mathbf{E}_b(t)$, and compares it to the lightning electric field change computed by the first method (T1) where rotation effects were neglected. For this particular flash, the Esonde undergoes nearly 50 degrees of rotation during the 1.3 s depicted in Figure 16. As can be seen in Figure 15, both techniques (T1) and (T2) yield about the same values for the lightning electric field change, even with a 50 degree rotation in the Esonde. Since the rotation speed was relatively constant, the underlying assumption for (T1) that the background could be approximated by a low-degree polynomial was valid.

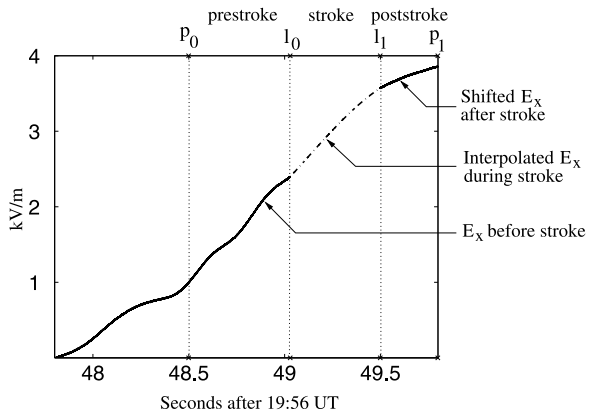

Figure 12. Background electric field $\mathbf{E}_b$ corresponding to E_x in Figure 11.

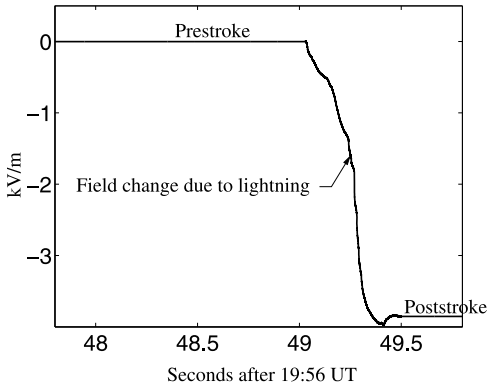

Figure 13. The x component of the electric field change $\mathbf{E}_L$ due to lightning. This is obtained by subtracting the background shown in Figure 12 from $\mathbf{E}_m$ shown in Figure 11.

[33] Since the Esonde hangs in a relatively vertical position, the rotation matrix in (7) has the following structure:

$$\mathbf{R}(t) = \begin{bmatrix} \cos\theta(t) & -\sin\theta(t) & 0 \\ \sin\theta(t) & \cos\theta(t) & 0 \\ 0 & 0 & 1 \end{bmatrix},$$

where θ is the rotation angle. Consequently, the z component of $\mathbf{c}_0$ in (7) cancels on the left side of the equation, and it is not possible to compute the z component of $\mathbf{E}_p$. Hence, the number of unknowns parameters on the left side of (7) is at most 8. Moreover, if the Esonde is relatively stationary, then $\mathbf{R}(t) = \mathbf{R}(0)$ to first order, and the entire $\mathbf{c}_0$ vector cancels in (7). Thus increasing the rotation of the Esonde improves the conditioning of the equations (7). As the rotation tends to zero, the equations (7) become more ill conditioned, and the error in our estimate for $\mathbf{E}_L$ increases.

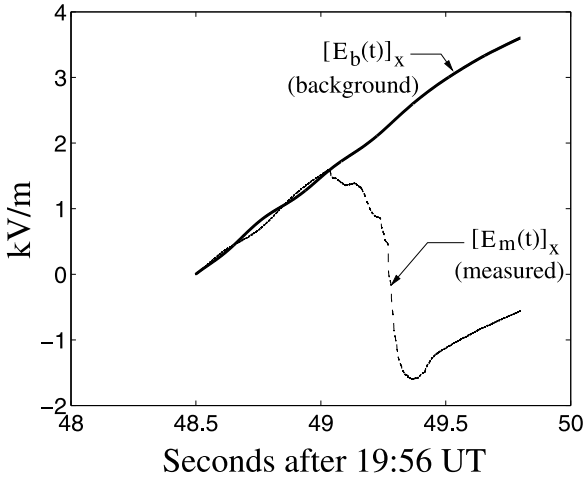

Figure 14. The x component of background field $\mathbf{E}_b$ (solid line) and the x component of $\mathbf{E}_m$ (dashed line) with time origin 1956:48.5 UT. The background was obtained by approximating $\mathbf{E}_p$, the slowly varying electric field, with a linear function of time whose coefficients are estimated by a least squares process.

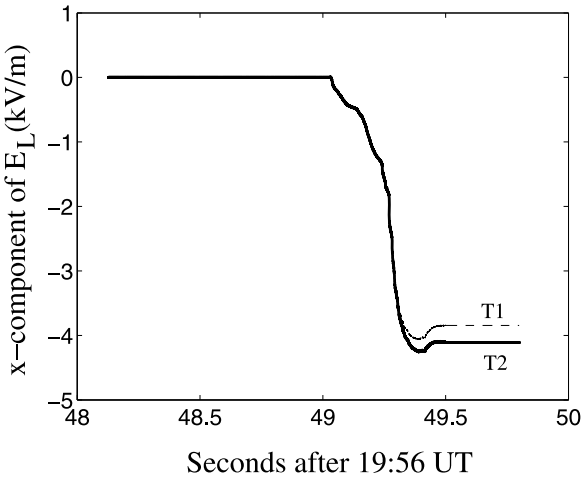

Figure 15. The x component of lightning electric field change computed by method (T1) described in section 4.1 (dashed line) and by method (T2) described in section 4.2 (solid line). The (T2) curve is obtained by subtracting the background solid curve from the measured dashed curve in Figure 14.

[34] An advantage of the new technique for inverting the voltage measurement to obtain the electric field is that we obtain horizontal components of both $\mathbf{E}_L$ and $\mathbf{E}_p$, while the previous technique computes the electric field change $\mathbf{E}_L$ without obtaining an estimate for $\mathbf{E}_p$. Since the total $\mathbf{E}$ field at the Esonde is the sum $\mathbf{E}_L + \mathbf{E}_p$ (see (3)), the new technique yields the horizontal component of $\mathbf{E}$ at the Esonde. In Figure 17, we show the horizontal $\mathbf{E}$ as a function of time, both before and after the IC flash of 1956 UT. Notice that the flash results in more than a 65 degree rotation in the horizontal electric field at the Esonde.

4.3. IC Charge Transport Analysis

[35] The techniques for determining the charge transport in a flash were developed by *Hager et al.* [2007]; here we summarize the techniques. To make the discussion more concrete, we consider a specific flash, an IC denoted Flash 2, whose LMA pulses appear in Figures 18 and 19. For an IC, we compute the best dipole fit to the measured electric field at the Esonde which satisfies various physical constraints that are designed to exclude unrealistic dipole fits. First, we require conservation of charge and we constrain the charge movement to the lightning channel revealed by the LMA pulses. Often, there are many ways to fit the measured electric fields while satisfying the channel constraint, so we need additional conditions to exclude the nonphysical fits. One constraint is that the dipole charge centers are separated by several kilometers since it is always easy to fit the electric fields using close, nonphysical, dipole centers. For Flash 2, we found that even with the separation constraint, there were two different mathematical fits to the data. One placed the dipole charge center for the origin of the charge transport at 13 km altitude, while the other fit placed the charge center at 8.5 km altitude. Since the 13 km altitude was implausible, we constrained the altitude of this dipole charge center to be at most 10 km. The best fit, subject to this additional constraint, was achieved with the dipole charge center at an altitude of 8.5 km.

[36] Further refinements in the locations of dipole charge centers were obtained through a statistical process developed by *Hager et al.* [2007], based on the estimated uncertainty in instrument gains. Each choice of the gains in the intervals of uncertainty gave a different best fitting location for the dipole charge centers. After trying many different values for the gains in the intervals of uncertainty, certain charge locations are found to be highly likely while other locations were unlikely. These unlikely locations could be far away from the likely locations, and the charge transport could be very abnormal. Additional constraints are added to exclude these unlikely charge center locations (outliers). Our final best fit is the average best dipole fit which satisfies all the constraints (the statistical constraints, the channel constraints, the separation constraints, and charge conservation). The averaging is performed over all choices for the instrument gains in the intervals of uncertainty. For a more detailed discussion of the fitting process, see *Hager et al.* [2007].

4.4. CG Charge Transport and Stroke Multiplicity

[37] The return stroke of a CG flash causes a jump in the electric field record. Hence, the strokes of a CG flash correspond to the jumps in the electric field record. The stroke multiplicity for CGs was determined by analyzing the electric field record and by counting the number of return strokes.

[38] The fit process for a CG flash is similar to that for an IC flash, but instead of using dipoles, we try to fit each stroke of the CG using a monopole. Charge transport in a CG flash is often much easier to analyze than in an IC due to the short time duration of the return stroke during which the transport takes place; hence, the error due to instrument rotation is essentially negligible. An exception to this is the charge transport during a continuing current phase which might last 0.1 s, and which requires more careful analysis. A detailed study of an eight-stroke CG flash is provided by *Hager et al.* [2007].

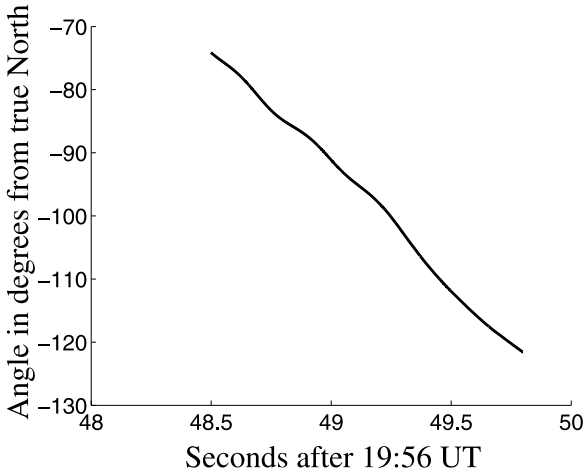

Figure 16. Rotation angle of the Esonde relative to true north.

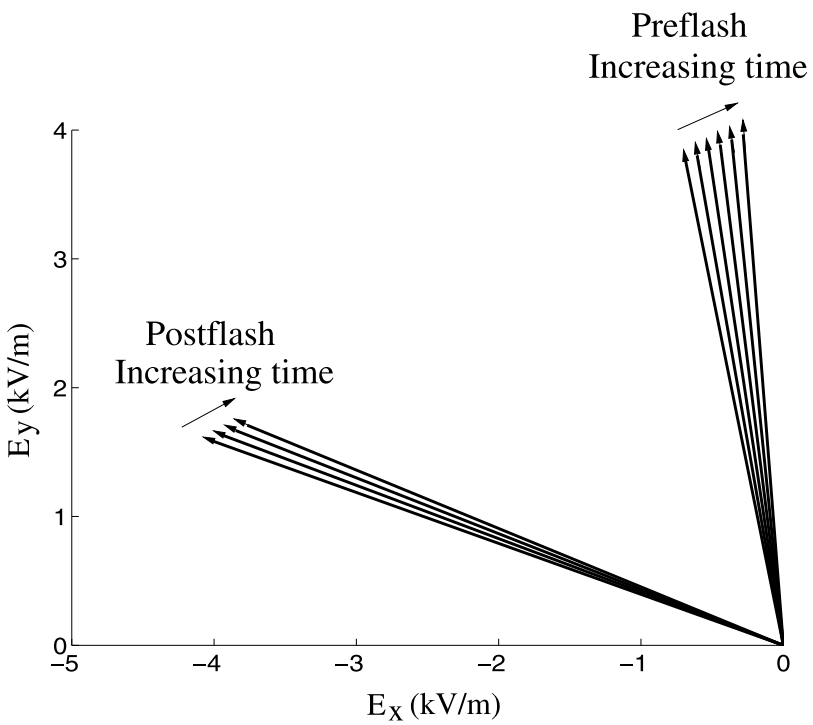

Figure 17. Horizontal electric field for the flash of 18 August 2004, 1956 UT. Before the flash, the horizontal field points to the north; the flash causes the field to rotate more than 65 degrees counterclockwise.

4.5. Limitations in the Analysis

[39] Although there were 190 flashes (41 CGs and 149 ICs) within 15 km of the balloon, we were only able to analyze 24 flashes (9 ICs and 15 CGs with 44 strokes). Hence, 166 flashes could not be analyzed. We could not analyze flashes for the following reasons.

[40] 1. The data were incomplete. As explained by *Sonnenfeld et al.* [2006], the Esonde flown in 2004 operated in 3.0 s cycles. During the first 2.0 s of the cycle, data are acquired by the computer, while during the last 1.0 s, there is no data acquisition as the computer wrote to the compact flash memory card. Unless the entire flash occurred during the 2.0 s data cycle, it was not possible to analyze charge transport.

[41] 2. The electric field change could not be reliably measured since either the charge transport was far from the Esonde or the dipole charge centers were relatively close together.

[42] 3. Electrode(s) on the instrument became charged due to collisions with cloud particles. These instrument anomalies are usually obvious when inspecting the data.

[43] 4. The flash was too complex to model using the measured three components of the electric field at the Esonde. For example, a flash may contain forks which draw charge from many different regions in the cloud and a monopole or dipole fit may be inappropriate. Hence, the monopole and dipole constraints in the charge transport analysis delineate a class of flashes that can be analyzed with the available data. The more complex flashes with charge being transported from many different regions in the cloud at once were outside the scope of our analysis.

[44] In most cases, a flash was not analyzed due to reasons 1, 2, or 3. Even when a flash covers a large area, it was often possible to approximate the overall charge movement using either a monopole or a dipole model. However, as the complexity of the flash increases, the quality of the approximation becomes worse. We only consider flashes and strokes where the relative error in a monopole or a dipole fit is on the order of 5% or less.

5. Analysis of Noteworthy Flashes

[45] This section analyzes the charge transport for five specific flashes which occurred during the thunderstorm of 18 August 2004. The flashes are presented in chronological order.

5.1. Flash 1, Updraft Flash, 1956:48 UT

[46] Flash 1, located near U1, is referred to as an "updraft flash" since the flash was located near the updraft and the lightning channel propagates so as to connect the positive charge at the top of the updraft to the negative charge below. Figure 18 (top) shows the projection of the LMA pulses on the *xz* plane. The pulses are color coded based on the time since the start of the flash (blue is the beginning of the flash, while red is the end of the flash 0.5 s later). The square in Figure 6 (bottom left) shows the location of Flash 1 in the N3R radar plot which starts at 1959:35 UT. As can be seen, Flash 1 has nearly the same location as the reflectivity core. A similar vertical flash is described in detail by *Shao and Krehbiel* [1996] [see also *Scott et al.*, 1995; *MacGorman and Rust*, 1998, p. 199], where the authors give both interferometer observations of the flash and dual-polarization radar measurements. The authors' radar measurements in

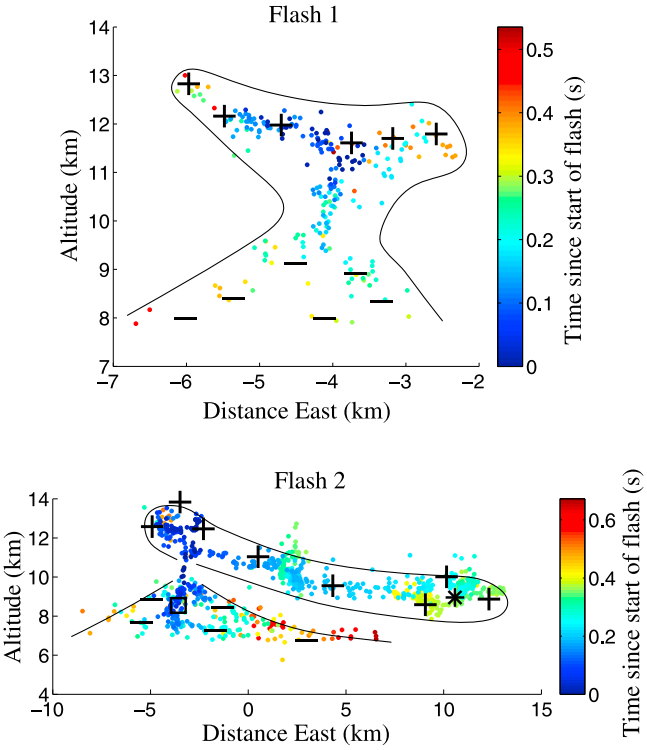

Figure 18. (top) Projection on the *xz* plane of the LMA pulses for a flash, denoted Flash 1, which occurred within the updraft U1 at 1956:48 UT. (bottom) The same *xz* projection for Flash 2, which occurred at approximately 2007:47 UT. In both plots, LMA pulses are color coded on the basis of time since start of flash; the inferred signs of the cloud charges are indicated by pluses and minuses. The best fitting dipole charge centers for Flash 2 are indicated by a square (charge center in region of negative cloud charge) and by an asterisk (charge center in region of positive cloud charge). We infer that the cloud charge at the eastern end of the channel is positive since 20 C electrons were transported to the region near the asterisk; similarly, the cloud charge near the square is negative since this was the origin of the charge which neutralized the positive ions at the end of the channel. The top of the updraft is positively charged. Both Flash 1 and Flash 2 initiate near U1. Flash 2, however, occurs 11 min after Flash 1.

that study implied that the ice crystals, and hence the electric field, were aligned vertically in the middle part of the flash.

[47] Flash 1 in Figure 18 appears to move negative charge from an altitude around 8 km up to 13 km. The electric field change at the Esonde is relatively small since this flash is about 20 km away from the instrument. Nonetheless, it is possible to estimate the charge transfer. The change in the vertical electric field at the Esonde is about 100 V/m. Based on the analysis of other flashes, such as Flash 2, the center of negative charge in the updraft is about 8.5 km. The center of positive charge in Figure 18 appears to be around 12 km. Taking into account the location of the ground plane under the flash, we conclude that the charge transport is about 26 coulomb (C).

5.2. Flash 2, Extensive Flash, 2007:47 UT

[48] Until about 15 min after the initiation of U1 around 1951 UT, most flashes associated with U1 were updraft

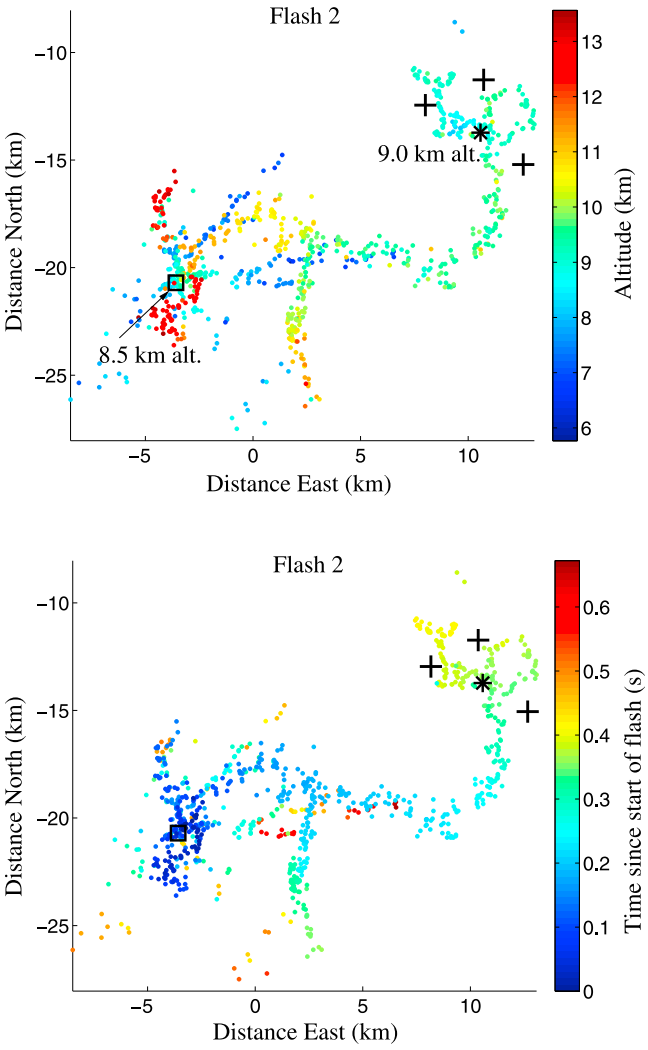

Figure 19. LMA pulses for Flash 2 projected into the *xy* plane (top) color coded on the basis of pulse height above sea level and (bottom) color coded on the basis of time since the start of the flash, which occurred at approximately 2007:47 UT. We infer that the sign of the cloud charge on the east end of the lightning channel is positive as indicated by the pluses. The axes give the distance north and east of Langmuir Laboratory. The best fitting dipole charge centers are indicated by a square (charge center in region of negative cloud charge) and by an asterisk (charge center in region of positive cloud charge). The altitude of each charge center is labeled. The red dots in Figure 19 (top) correspond to LMA pulses near the top of the updraft, where the cloud charge is positive. The blue dots adjacent to red dots are associated with lower altitude LMA pulses where the cloud charge is negative. The *xz* projection in Figure 18 (bottom) gives a clearer view of the charge separation.

flashes. Between 2005 UT and 2015 UT, the lightning discharge pattern around U1 undergoes a fundamental change as the number of updraft flashes decreases, and *extensive* flashes become predominant. We define an extensive flash as one which propagates from a region of negative charge to a region of positive charge which has a relatively large spatial extent. For the flashes that we analyzed, the positive charge region consisted of a large volume of positive charge at the top of the updraft which was connected by a positive layer to another volume of positive charge 10 to 20 km away.

[49] The LMA plots for Flash 2, an extensive flash which occurs at 2007:47 UT, are given in Figure 19 and in Figure 18 (bottom). In the *xz* projection shown in Figure 18 (bottom) the separation between the positive (upper) and negative (lower) charge layers is indicated by the plus and minus signs. Figure 19 (top) gives the projection of the LMA pulses into the *xy* plane with the pulse color based on altitude; red corresponds to 13 km altitude, while blue corresponds to 6 km altitude (see colorbar on right side of plot). In Figure 19 (bottom) the pulses are colored according to the pulse time relative to the start of the flash. Perspective views of this flash along with an animated tour around the flash are available in the auxiliary material (Figures S5 and S6 and Animation S4).

[50] The analysis of Flash 2 indicates that about 20 C negative charge is moved from the southwest end of the flash to the northeast end. The location of the dipole charge centers are indicated in the LMA plots (Figures 18 and 19). The charge center in the region of positive cloud charge is an asterisk while the center in the region of negative cloud charge is a box. As can be seen in the LMA plots, charge is moved over a 15 km by 15 km region. A dipole is essentially a first-order approximation to the charge movement. Obviously, some charge must have been deposited at the top of the thundercloud (the bright red dots in Figure 19 (top) and the highest dots in Figure 18 (bottom)), and some charge must have been deposited on the less elevated north/south channel, between 2 and 3 km east; however, in our dipole approximation, all the charge moves to a spot on the eastern end of the channel at 9 km altitude. Since this dipole approximation matches the electric field data with an error of less than 1%, we believe that much of the charge transport took place between the two charge centers indicated in Figures 18 and 19. Comparing Figure 18 (top) and Figure 18 (bottom), we see the huge difference between the size of Flash 1 and Flash 2. The width of Flash 1, the updraft flash, is 5 km while the width of Flash 2, the extensive flash, is 25 km. The span of an extensive flash can be 10 to 25 km even in the relatively compact mountain storm we are studying.

[51] The 2007:26 UT composite radar reflectivity (see Figure 4) has the closest temporal proximity to Flash 2 (2007:47 UT). The dipole charge center in the positive region is situated in the 35 dB*Z* (yellow) pixels immediately southeast of the balloon, while the dipole charge center in the negative region lies in the intense 65 dB*Z* (red/purple) cell southwest of the balloon. In Figure 6 these dipole charge centers are superimposed on the 2010 UT N3R radar reflectivity image. As seen in Figure 18, the LMA pulses approach 14 km in altitude in the positive region located right above the dipole charge center in the negative region. The location of these high-altitude LMA pulses (Figure 9) coincides with the reflectivity core in the N3R scan seen in Figure 6.

[52] Notice in the LMA record for Flash 2 that there is a high branch of LMA pulses running north/south between 2 and 3 km east (see Figure 19 (top)). In Figure 18 (bottom) this high branch corresponds to the green protruding dots between 2 and 3 km east. As we observed in Figure 9, U2 seemed to develop a downwind ring of charge associated with the high LMA pulses. U1 is also developing a downwind charge region. As the Flash 2 channel propagates toward the positive charge region on the east side of Figure 19, it also sends a branch south which neutralizes downwind positive charge.

5.3. Flash 3, IC/CG, 2013:08 UT

[53] Next, we analyze a flash, denoted Flash 3, which occurred on the east side of our study region. The projection on the *xy* plane of the LMA pulses for Flash 3 is shown in Figure 20. The pulses are colored by altitude in Figure 20 (top) and by time in Figure 20 (bottom).

[54] Figure 20 actually depicts two flashes which we denote Flash 3.1 and Flash 3.2. Flash 3.1 is an IC which travels along the north/south channel of Figure 20, starting at the north end near the square (dark blue dots in Figure 20 (bottom) and low-altitude blue dots in Figure 20 (top)) and sweeping through the asterisk to the south (light blue dots Figure 20 (bottom) and high-altitude red dots in Figure 20 (top)). The classification of Flash 3.2, which occurs after Flash 3.1, is ambiguous as explained below. Flash 3.2 propagates toward the southwest in the direction of the circle.

[55] The National Lightning and Detection Network (NLDN) record for Flash 3 indicates a negative CG at the time of Flash 3.1, the IC. The strike point, a few kilometers northeast of the LMA pulses in Figure 20, has a median expected error of 9 km and the Chi-squared value is 3, indicating that a CG is a very poor fit to the measured wave forms. Hence, it is likely that this is a poorly located and misclassified cloud pulse, as described by *Fleenor et al.* [2009] and reiterated by *Cummins and Murphy* [2009].

[56] The *z* component of the electric field for this flash is shown in Figure 21 (top). The electric field rises, remains roughly constant, and then drops. The initial rise in the electric field is associated with a normal polarity IC flash. The rise in the electric field corresponds to the blue dots in Figure 20 (bottom). During the rise in electric field, LMA pulses propagate southward from lower altitudes around the box in Figure 20 to upper altitudes near the asterisk, marching to the end of the north/south channel.

[57] The increase in the vertical component of the electric field during Flash 3.1 can be explained as follows: The Esonde was positioned about 10 km northwest of Flash 3, about 2 km closer to the asterisk (positive cloud charge) than to the square (negative cloud charge). The altitude of the Esonde was about 4.1 km while the altitude of the asterisk is 8.8 km. As a result of this altitude differential, the electric field vector at the Esonde due to the lightning has a substantial vertical component. It is this upward pointing E from the charge transport of the flash which causes the vertical E to increase during Flash 3.1.

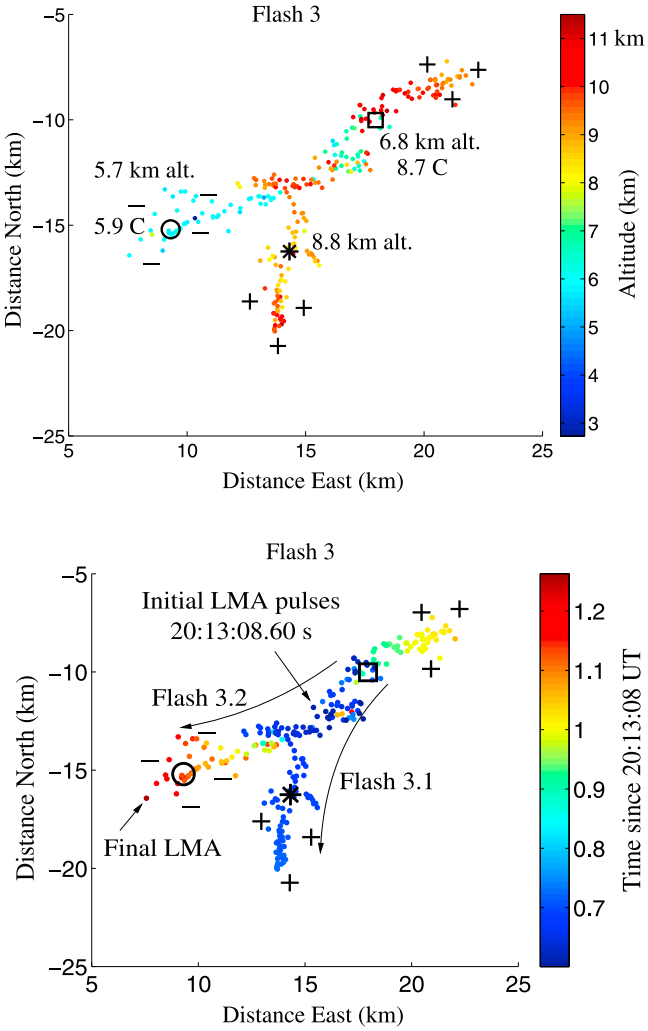

Figure 20. LMA pulses for Flash 3 which occurred at approximately 2013:08 UT. Projection of the LMA pulses into the *xy* plane, with (top) colors based on the altitude and (bottom) colors based on the time since the start of the flash. The inferred signs of the cloud charges are indicated by pluses and minuses. The axes give the distance north and east of Langmuir Laboratory. The positive and negative charge at the ends of channel segments are indicated. The red and yellow dots in Figure 20 (top) correspond to the positive layer, while the blue dots correspond to the negative layer. The best fitting dipole charge centers for the initial IC component of the flash, Flash 3.1, are indicated by a square in the region of negative cloud charge and by an asterisk in the region of positive cloud charge. In Flash 3.2, 5.9 C charge are removed from the lower negative region; the charge center is circled. We could not uniquely determine the other dipole charge center. Both the ground and the high northeast end of the channel fit the measured electric field change.

[58] The second part of Flash 3, denoted Flash 3.2, is quite interesting and a bit puzzling; the steps in the electric field seen in the Figure 21 (bottom) are separated by 0.02 to 0.03 s. The charge transport analysis for Flash 3.2 shows that 5.9 C of negative charge is removed from the region indicated by the circle in Figure 20. The analysis, however, does not uniquely specify the destination of the charge. The measured electric field is matched by either transporting the charge to ground or by transporting the charge to the northeast end of the high-altitude channel (see Figure 20 (top)). A likely interpretation of the steps in the electric field are that they are K changes [*Rakov and Uman*, 2003, section 9.5], which characteristically occur late in the development of an IC flash. However, the LMA record is ambiguous.

[59] In Figure 21 (bottom) we mark seven jumps in the electric field, and in Figure 22, we plot the altitude of the LMA pulses versus time. The pulses up to 0.75 s correspond to Flash 3.1, the IC which transfers 8.7 C charge from the box to the asterisk in Figure 20. The LMA record is quiet for 0.1 s before Flash 3.2 starts. From the start of Flash 3.2 until about 1.03 s in Figure 22 (top), we see LMA pulses at

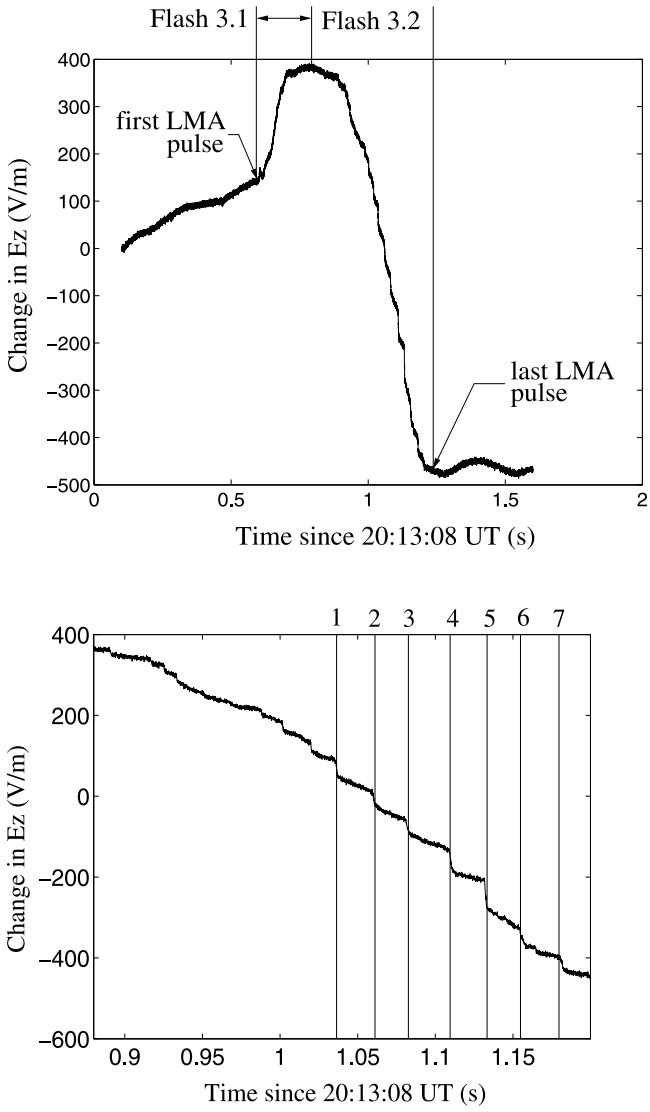

Figure 21. The *z* component of the electric field change as a function of time for Flash 3. In Figure 21 (bottom) we expand the portion of Figure 21 (top) corresponding to the drop in the electric field. Seven jumps in the electric field are marked in Figure 21 (bottom) and in Figure 22.

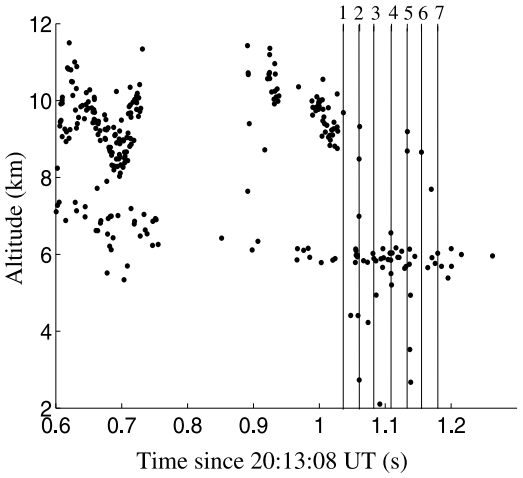

Figure 22. Altitude of the LMA pulses for Flash 3 versus time after 2013:08 UT. The seven times marked in the plot correspond to the seven times marked in Figure 21.

both 6 km altitude and at 10 km altitude. Hence, the initial drop in the electric field seems to be connected with an IC whose LMA pulses propagate along the northern channel in Figure 20. However, at the time labeled 2 in Figure 22, there are six LMA pulses in quick succession around 6 km in altitude (only four are visible in Figure 22 (bottom) due to the superposition of dots), and then two LMA pulses propagate to ground and three pulses propagate to high altitudes. The lowest pulse at 2730 m altitude is 10 LMA station data while the higher pulse at 4410 m is 9 station data. Also, just beyond the time labeled 5, we see a series of five pulses propagate to ground. It is not clear whether the LMA pulses near ground are simply noise, or something else not understood. It continues to be interesting to combine measurements from LMA and the electric field aloft; we expect in time to have sufficient database to better understand an unusual flash signature like that of Flash 3.

5.4. Flash 4, IC, Late Updraft Flash, 2017:54

[60] Figure 23 shows the LMA pulses for Flash 4 in the *xy* plane (Figure 23 (bottom)) and *xz* plane (Figure 23 (top)). The dipole charge centers for this flash were too close together to determine the charge transport. Flash 4 is much smaller than Flash 2, but related to it. In Figure 19 we see that Flash 2 has a north/south channel segment around 3 km east and −25 km north. According to Figure 23, this is where Flash 4 originates. Flash 4 starts in a lower negative charge region at 3 km east and −25 km north, it propagates upward into a higher positive region and then travels northwest and higher toward the top of U1, whose center, as estimated from radar reflectivity, is indicated by a diamond in Figure 23. Like Flash 1, this is an updraft flash since it is located near U1 and it propagates between the top of the updraft and the negative charge layer below. Comparing the size of this updraft flash to Flash 1, which occurred about 21 min earlier, we see that Flash 4 extends over about 6 km, while Flash 1 extends over about 4 km.

5.5. Flash 5, Extensive Flash, 2021:30 UT

[61] An interesting flash, denoted Flash 5, originates near U2. The *xy* view of the LMA pulses is given in Figure 24 (bottom), color coded by altitude. The location of the dipole charge centers are indicated by an asterisk and a square. U2 lies on the north side of the flash near the highest LMA pulses. The *xz* view of the LMA pulses in the Figure 24 (top) reveals the separation between the lower negative and upper positive regions. Flash 5 is particularly interesting since the dipole charge center in the region where cloud charge is negative is slightly higher than the charge center in the region where cloud charge is positive (7.7 km altitude versus 7.6 km altitude). As can be seen in Figure 24, the positive charge region is always above the negative charge region, however, the analysis shows that much of the transported negative charge came from the high, negative, eastern

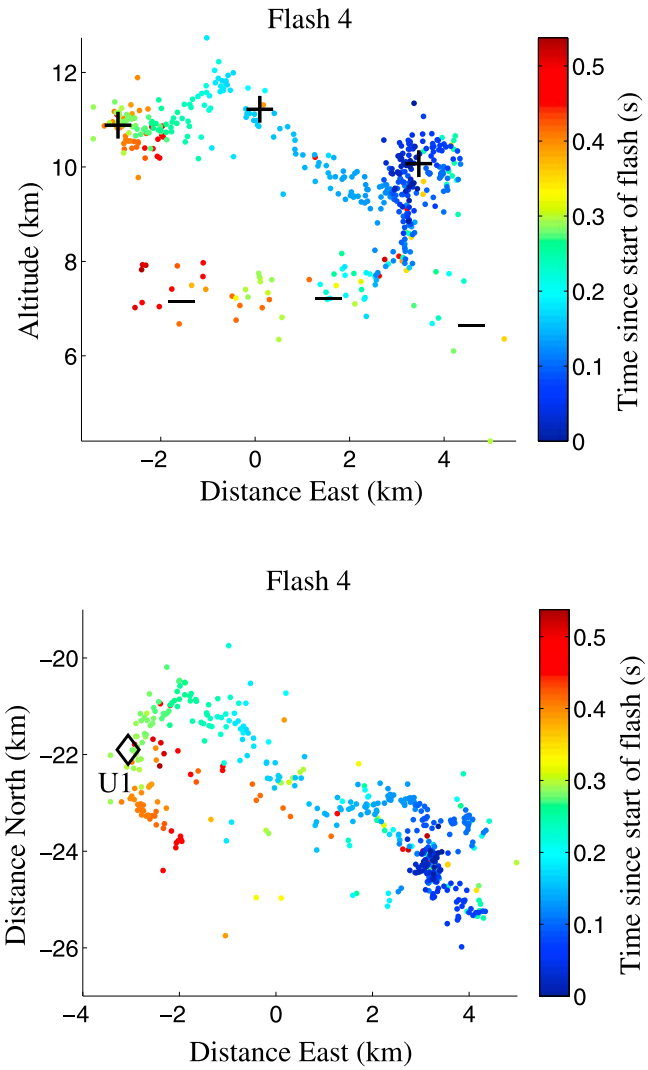

Figure 23. LMA pulses for Flash 4 which occurred at approximately 2017:54 UT. (top) The *xz* projection and (bottom) the *xy* projection. The colors show the pulse time relative to the start of the flash. The inferred signs of the cloud charges are indicated by pluses and minuses. The diamond is the mean location of U1.

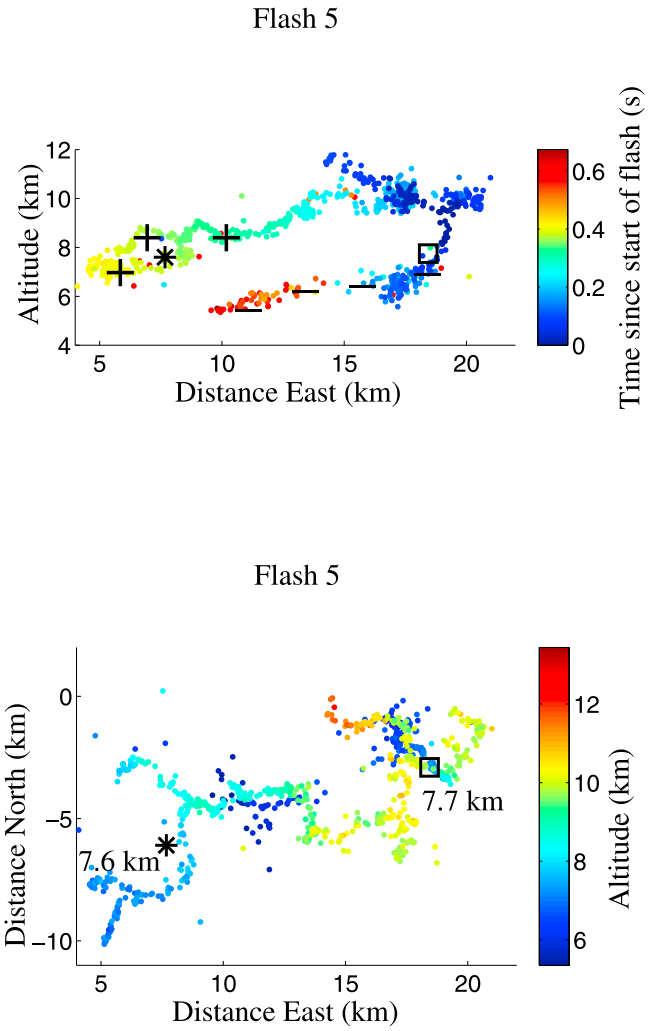

Figure 24. LMA pulses for Flash 5, which occurred at approximately 2021:30 UT. (top) Projection on the *xz* plane, color coded by altitude, and (bottom) projection on the *xy* plane, color coded by pulse time relative to the start of the flash. The inferred signs of the cloud charges are indicated by pluses and minuses. The dipole charge centers are indicated by a square (center in region of negative cloud charge) and an asterisk (center in region of positive cloud charge). The altitude of each charge center is labeled.

end of the flash, and the charge was transported to the lower, western end in the positive layer.

6. Charge Transport Analysis

[62] In this section we analyze the charge transport data to ascertain the location of electron sources and sinks and to develop the discharging structure of the storm. As mentioned in section 5, the discharge pattern associated with U1 undergoes a fundamental change between 2005 UT and 2015 UT. The number of updraft and extensive flashes associated with U1, as a function of time, is shown in Figure 25. Figure 25 shows that between 1955 UT and 2010 UT, most of the flashes connected with U1 were updraft flashes. Between 2010 UT and 2015 UT, the number of updraft flashes is nearly zero and the extensive flashes are predominant.

[63] Figure 26 shows the charge transport in the *xy* plane for the flashes that we analyzed. We show the location of the two updraft flashes, F_1 and F_4, while the remaining flashes are either CG strokes or extensive IC flashes. The area of each circle in Figure 26 is proportional to the magnitude of the charge transferred. In a dipole, the end in the region of positive cloud charge is indicated by an asterisk, while a circle marks the end in the region of negative cloud charge. A solid line connects the dipole charge centers. The color of each monopole or dipole indicates the altitude of the charge center (see altitude scale on the right side of Figure 26). The mean locations of U1 and U2 (given in Figure 7) are marked by diamonds. The trajectory of the balloon-borne Esonde is the dark curve in the middle of Figure 26. The northwest end of the trajectory is Langmuir Laboratory. Since the balloon is carried by the wind, the balloon trajectory indicates the wind direction at the altitude of the balloon. All the numerical data which are plotted in Figure 26 are available in the auxiliary material (Data Set S1).

[64] In Figure 27 we view the data of Figure 26 from the west. Observe that the charge centers in the positive region (red) all lie above the charge centers in the negative region (blue) when viewed from a direction perpendicular to the wind flow.

[65] The flashes that were analyzed in section 5 are labeled F_1 through F_5 in Figure 26. The IC flashes analyzed by *Hager et al.* [2007] are labeled I_1 and I_2. The positive charge centers at the north end of Figure 26 reflect charge transport to the northern cells labeled U3 in Figure 3 (reflectivity cores northeast of Langmuir Laboratory in Figure 6). The positive charge centers on the west side of Figure 26 reflect charge transport to a western cell labeled U4 in Figure 3 (the reflectivity core west of Langmuir Laboratory in the 1933 UT image of Figure 6).

[66] It is important to note that the data presented in Figure 26 correspond to flashes that we could analyze. These were extensive flashes and CGs that were generally near the Esonde so that the electric field change could be estimated reliably. Although the number of updraft flashes is comparable to the number of extensive flashes, we were

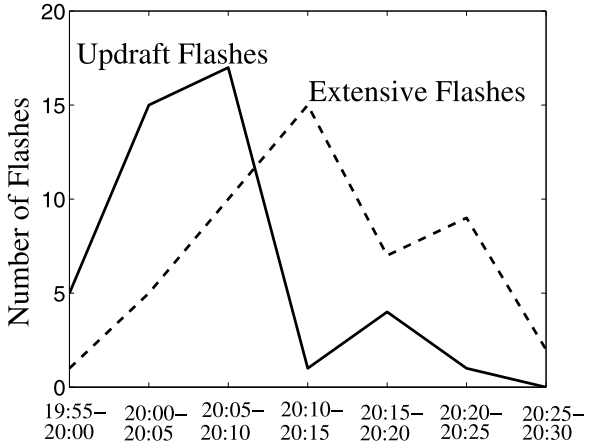

Figure 25. Number of updraft and extensive flashes associated with U1 in each 5 min time interval between 1955 UT and 2030 UT.

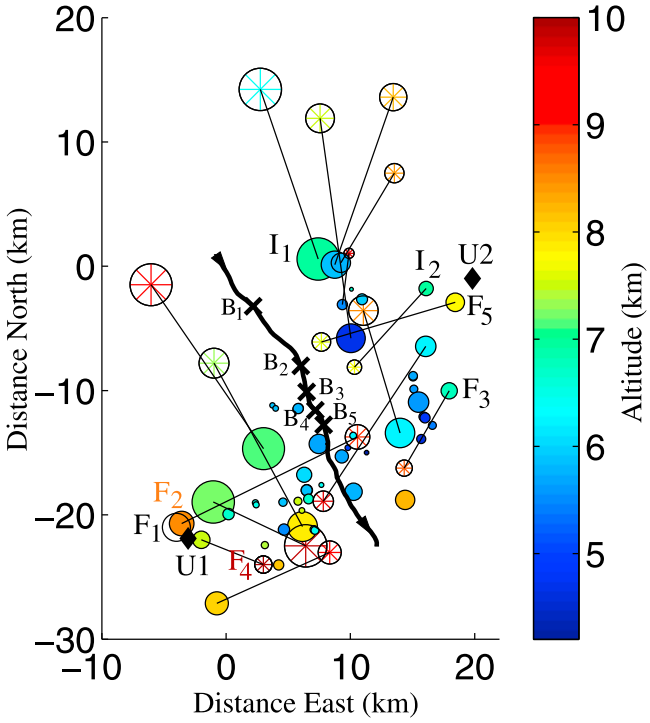

Figure 26. Monopole and dipole charge centers for the 9 ICs and 44 strokes associated with 15 CGs that were analyzed. An asterisk marks the dipole center in the region of positive cloud charge, and a circle marks the dipole charge center in the region of negative cloud charge. The axes give the distance north and east of Langmuir Laboratory. The area of each circle is proportional to the amplitude of charge transport, while the color is proportional to altitude (see color code on right). Diamonds mark the mean location of U1 and U2. The track of the balloon-borne Esonde, starting at Langmuir Laboratory, follows the black curve, with arrows indicating the flight direction. The location of the balloon at the time of each of the five flashes is marked by a cross and labeled B_1 through B_5. The charge transport for Flash 4 is simply a guess since this flash was not analyzed; the two circles for Flash 4 simply mark the extent of the LMA pulses. The circle corresponding to Flash 1 is not filled in so as to avoid covering the circle for Flash 2. For Flash 1, the two charge centers are located on top of each other.

unable to analyze updraft flashes using the same techniques since they were too far from the Esonde and the charge centers were too close together. Nonetheless, as we saw with Flash 1, by making plausible assumptions concerning the location of the charge centers, we can estimate the charge transport. For Flash 1, the estimated charge transport was 26 C while the average charge transport for the IC flashes in Figure 26 is 25.2 C. Hence, these updraft flashes represent a significant amount of charge transport, comparable to that of the extensive IC flashes in Figure 26. In developing a picture for the charge sources and sinks, we must remember that much negative charge is constantly flowing to the top of the updraft through updraft flashes, such as Flashes 1 and 4, while Figure 26 does not account for this negative charge flow to the top of the updraft.

[67] The positive charge centers east of U1 in Figure 26 are all situated in the same general region near (10, −20) km. The reason that we see positive charge centers bunched together here is that this is a positive charge region which is near the balloon flight path; consequently, we were able to analyze the ICs with charge centers in this region.

[68] Flash 1 and Flash 2 are representative of the flash activity which originates near U1. Flash 1 transports negative charge to the top of U1, while Flash 2 transports negative charge away from U1. Figure 28 shows the density of LMA pulses in the *xy* plane between 2000 UT and 2030 UT. The density is computed as following: The region around U1 is partitioned into 100 m by 100 m pixels. In each pixel, we determine the number of LMA pulses. We then average the results for each pixel with its neighbors to remove noise. The peak pulse density is about 6400 pulses/km^2 in the middle of the red region near U1, while the density is relatively small elsewhere, from 800 pulses/km^2 down to zero. The region of high pulse density coincides with the intense reflectivity cores in Figure 6. *Taylor et al.* [1984] point out that CG flashes and large IC flashes are often closely associated with regions of high reflectivity.

[69] The pulse density plot, Figure 28, has the following interpretation: The density is highest near U1 since many flashes originate near U1, either updraft flashes located in or near the updraft or extensive flashes which originate near U1. The density is lower away from U1 since extensive flashes propagate away from U1, in many directions, and the LMA pulses are spread over a larger area. The pulses outside the updraft are nearly imperceptible in Figure 28 since their density is so small compared to the density of pulses inside the updraft.

[70] Figure 29 shows the density of pulses outside the updraft. This plot is obtained by ignoring the high-density region near the updraft and plotting the density in the complement. Since the pulse density is so low outside the updraft, it was necessary to increase the pixel size to 500 m by 500 m so that they would contain a significant number of LMA pulses. In Figure 29 we also show the location of the dipole charge centers in the region of positive cloud charge for the extensive flashes terminating near U1. Observe that

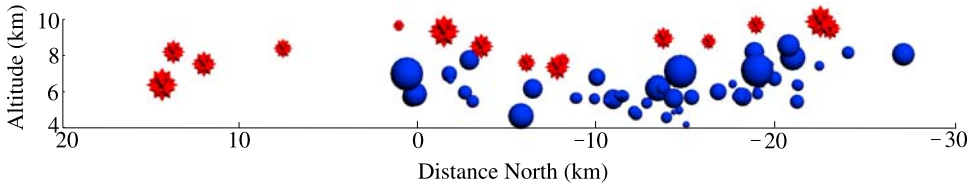

Figure 27. Monopole and dipole charge centers viewed from the west side of Figure 26. The charge centers in the positive region are red, while the charge centers in the negative region are blue.

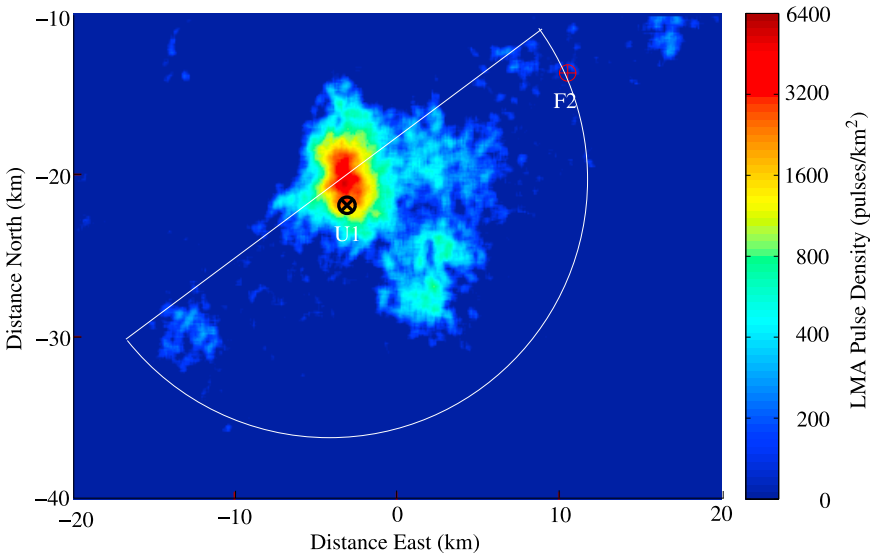

Figure 28. Density of LMA pulses between 2000 UT and 2030 UT. The mean location of U1, given in Figure 7, is marked with a black cross. The location of the charge center for Flash 2 in the region of positive cloud charge is indicated by a red plus. The axis of symmetry for the semicircle is in the direction of the prevailing wind.

these dipole charge centers tend to cluster on the edges of the region of highest density. These flashes originate near an updraft and then terminate 10 to 20 km outside the updraft. Note that the charge center outside the semicircle corresponds to a flash whose origin was the negative charge layer of U2.

[71] In Figures 28 and 29 we also plot a semicircle whose axis of symmetry is parallel to the direction of the wind. The circular side of the semicircle is downwind from the updraft. Note that many of the LMA pulses are contained in the semicircle, and the charge in the extensive flashes that we could analyze is transported away from the updraft and toward the edge of the semicircle. If other extensive flashes are similar to ones that we could analyze, the yellow/orange region in Figure 29 closest to the edge of semicircle would be positively charge at an altitude of 9 km.

[72] Figure 30 plots all the CG strokes reported by the National Lightning Detection Network (NLDN) during the time interval from 1950 UT to 2030 UT. We now compare the NLDN strike points to the origin of charge in the thundercloud as indicated in Figure 26. First observe that there are many CG charge centers northeast and east of U1 in Figure 26, but few south of U1. The reason for the small number of CG charge centers south of U1 is that CG flashes

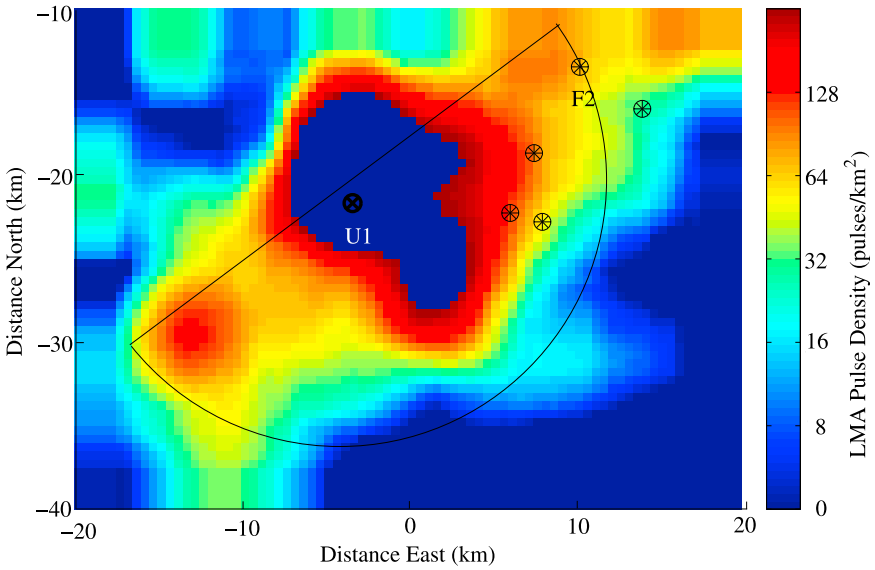

Figure 29. Density of LMA pulses between 2000 UT and 2030 UT after removing all LMA pulses near the updraft U1 (black cross). We show the location of the Flash 2 asterisk and nearby asterisks of Figure 26 which mark the dipole charge centers in the region of positive cloud charge.

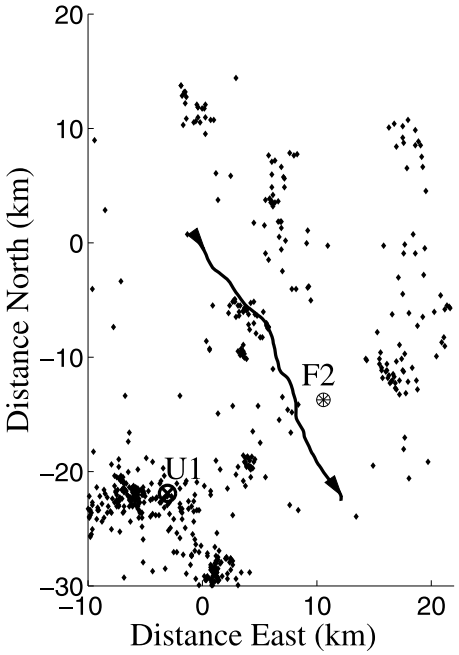

Figure 30. Lightning strike points reported by NLDN during the time interval from 1950 UT to 2030 UT. The balloon flight path, the mean location of U1, and the dipole charge center for Flash 2 in region of positive cloud charge are superimposed.

in this region were beyond the detection range of the Esonde. On the other hand, the NLDN plot in Figure 30 shows that there are even more CG flashes south and west of U1 than there were north (upwind) and east of U1.

[73] The NLDN data show the estimated strike points of CG strokes, while Figure 26 shows the origin of the charge in the cloud. Notice that there were no NLDN strikes reported near the asterisk for Flash 2 in Figure 30, while the charge transport analysis (Figure 26) shows a number of CG charge centers nearby. Thus the CG strike points on the ground were quite different from the origin of the associated negative charge in the cloud.

[74] We now plot the charge transport data in various ways in order to extract additional insight concerning the discharge structure. Figure 31 (top) shows the total positive charge (vertical axis) as a function of the distance north (horizontal axis). Figure 31 is generated as follows: We arrange a vertical slab 10 km thick which is perpendicular to the y axis and we add up all the positive charge enclosed by the slab. In Figure 31 (top) the horizontal axis is the location of the slab center relative to Langmuir Laboratory, and the vertical axis is the total positive charge enclosed by the slab. As seen in Figure 31, the positive charge achieves peaks around −20 km north, −5 km north, and 10 km north. The peak near −20 km north corresponds to U1. The peak at −5 km reflects positive charge associated with U2 and U4 (see Figure 3). The peak at 10 km is connected with charge transport to U3 cells north of Langmuir Laboratory.

[75] In Figure 31 (bottom) we plot the mean altitude of the positive charge derived from our charge transport analysis as a function of distance north. We compute the mean altitude as follows: For each choice of y between 30 km south and 20 km north, we average the altitude of all positive charge inside a vertical slab of width 10 km, perpendicular to the y axis, centered at this value for y. The mean altitude is highest near the energetic southern updraft U1. The mean altitude decreases as we move away from U1. As we approach the weaker northern updraft U2 near $y = 0$, the mean altitude increases. As we move north of U2, the mean altitude continues to decrease. As was seen in the radar, the storm cells travel from the northwest to the southeast. Hence, the storm cells north of Langmuir Laboratory are older than those to the south. The positive charge that was generated by these older storm cells has fallen to lower altitudes.

[76] In Figure 32 (top) we plot the mean altitude of the negative charge as a function of distance north. The left side

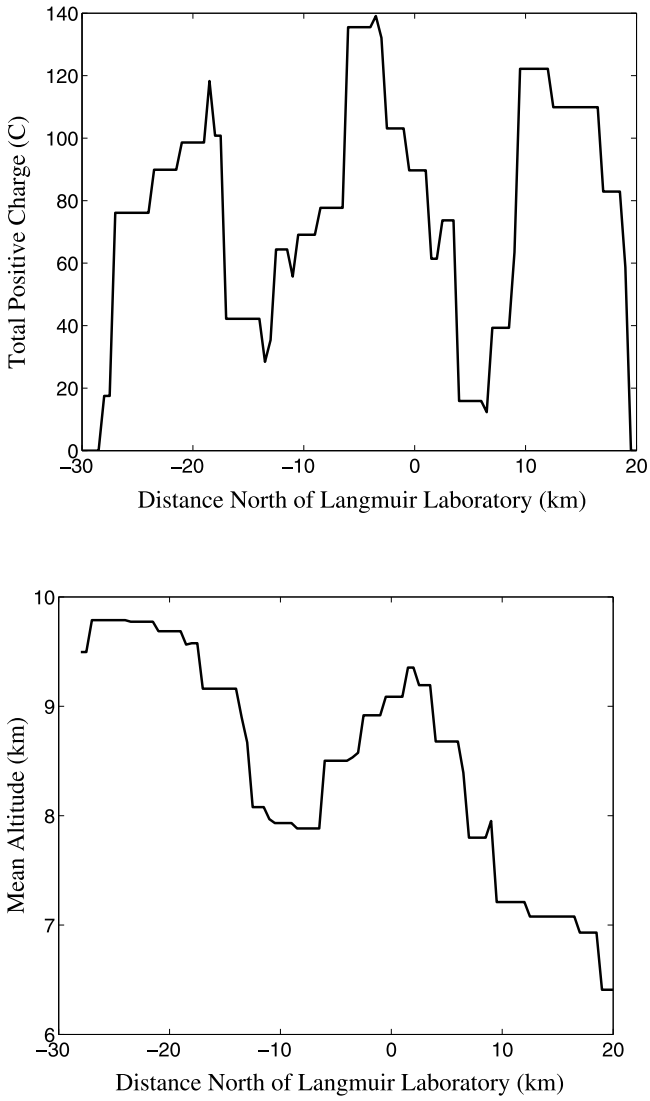

Figure 31. (top) Total positive charge versus distance north. The vertical axis give the sum of all charge in a vertical slab perpendicular to the y axis of width 10 km centered at the distance north shown on the horizontal axis. (bottom) Mean altitude of positive charge versus distance north. The mean is computed over a vertical slab perpendicular to the y axis of width 10 km centered at the distance north shown on the horizontal axis.

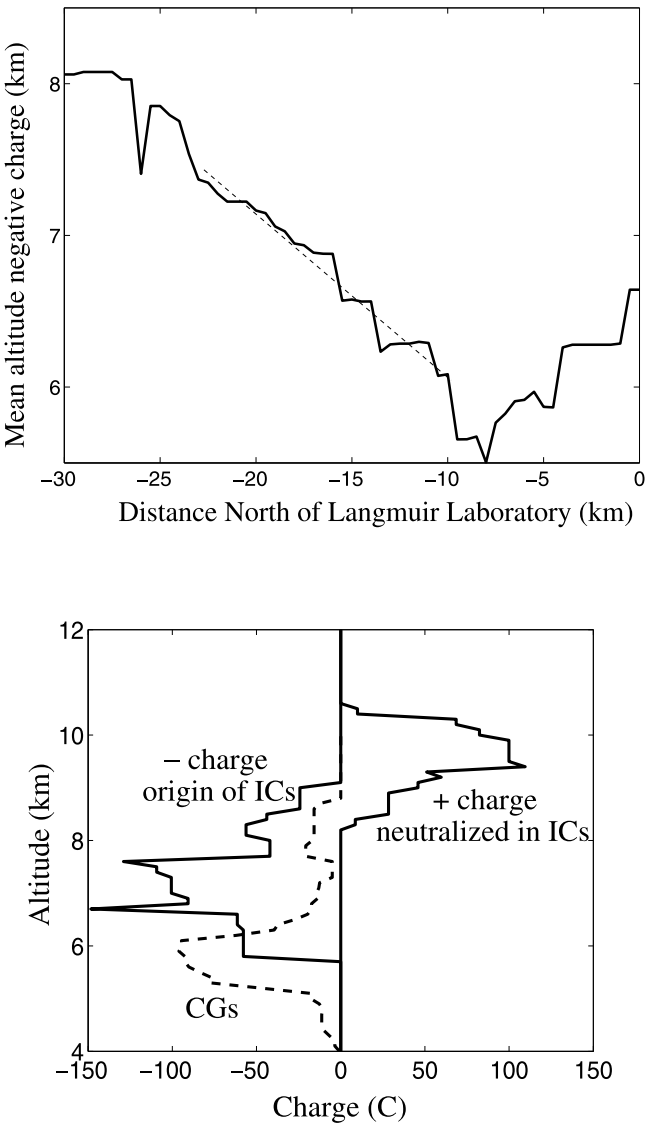

Figure 32. (top) Mean altitude of negative charge as function of distance north. The charge plotted is the sum of the negative charge transported by CGs and the negative charge of dipole centers at the origin ICs. The mean altitude is computed over a vertical slab of width 10 km centered at the distance north shown on the horizontal axis of the plot. The mean altitude decreases nearly linearly with distance from U1 over the interval [−23, −10]. (bottom) Charge versus altitude in the region at least 10 km south of Langmuir Laboratory which surrounds U1. Charge is obtained by summing contributions over a horizontal slab of width 1 km centered at the given altitude. The charge is partitioned into three categories: (1) the negative charge transported by CGs, (2) the negative charge associated with the dipole charge center at the origin of ICs, and (3) the positive charge which was neutralized by ICs.

of Figure 32 (top) corresponds to a location 30 km south of Langmuir Laboratory and slightly downwind from U1. Moving from left to right in Figure 32 (top) (south to north in the thunderstorm), the mean altitude of the negative charge first decreases as we move away from U1, then increases as we approach U2. The decrease in the mean altitude of negative charge as we move away from U1 also agrees with the decrease in LMA pulse altitude seen in Figure 10 and in Figure 18 (bottom). Notice that the mean altitude of the negative charge decays at a nearly linear rate relative to the distance from U1 from 10 to 23 km south of Langmuir Laboratory.

[77] In Figure 32 (bottom) we plot charge versus altitude for the region at least 10 km south of Langmuir Laboratory which surrounds U1. To compute the charge at any given altitude, we add together all charge contributions within a 1 km thick horizontal slab centered at the given altitude. The right side of Figure 32 (bottom) shows the positive charge which was neutralized by IC flashes. Observe that the positive charge has a unimodal distribution, reaching a peak at an elevation of 9.5 km. The negative charge on the left side of Figure 32 (bottom) is partitioned into the charge transported by CGs and the charge associated with the dipole charge center at the origin of ICs. Observe that the ICs generally transport negative charge from an altitude between 7 and 8 km, while most of the CGs transport negative charge from an altitude around 6 km. However, as can be seen in Figure 32, some CGs reach into the 8 km negative region closer to the updraft. Nonetheless, about 5 times as much charge is transported by CGs from the 6 km region as is transported by CGs from the 8 km region.

[78] Although there were more CG strokes than IC flashes, most of the charge in the thundercloud was transported by the IC flashes. In particular, the total charge transport by the ICs that we analyzed was 377.7 C while the total charge transport by the CGs that we analyzed was 141.9 C. The ratio 377.7/141.9 underestimates the true ratio since we were better able to analyze CG flashes than IC flashes. The ratio of the number of IC flashes to the number of CG flashes that we analyzed was $15/9 \approx 1.67$, while the ratio of the number of IC flashes to the number of CG flashes in the study region was 3.63. Hence, a better estimate for the ratio of IC charge transport to CG charge transport is given by

$$(377.7/141.9) \times (3.63/1.67) \approx 5.8.$$

Hence, nearly 6 times as much charge was moved by IC flashes compared to CG flashes.

[79] There were nine CGs with 44 total strokes, so each CG had about 4.9 strokes on average. The average charge transported in each CG flash was 15.7 C, while each CG stroke transported 3.2 C on average. Each IC, on the other hand, transported 25.2 C on average. Consequently, the ratio of average charge transport for an IC to average charge transport for a CG was 1.6.

[80] The charge transported by lightning emanates from the thunderstorm current generators. Using the lightning charge transport, we will estimate the generator current. In the study region, there were at least 149 IC flashes and 41 CG flashes between 1950 UT and 2030 UT. If we assume that the unanalyzed IC and CG flashes transported the same amount of charge, on average, as the analyzed flashes, then the total charge transport during 40 min of storm was 4399 C. We divide this by 2400 s to deduce that the charge transported by lightning requires a current of 1.8 Ampere (A). The total generator current is approximately the sum of lightning current and the conduction current, the current associated

with the neutralization of ions by electrons through conduction in the cloud. *Hager et al.* [1989] determined that for the TRIP storm of 11 July, 1978, at the Kennedy Space Center, the total generator current (lightning current plus conduction current) was about 1.3 times the lightning current. Hence, if this same factor 1.3 applies to the Langmuir Laboratory storm, then the total generator is about 2.3 A. For comparison, in the two-cell TRIP storm, the average generator current over 50 min of storm activity was 0.90 A, after correcting for the conduction current. Hence, this mountain storm was more active electrically than the Florida thunderstorm.

7. Conclusions

[81] The analysis of charge transport for a New Mexico mountain thunderstorm observed on 18 August, 2004, near Langmuir Laboratory, yielded the following insights concerning the electrical structure.

[82] 1. In the early stages of U1, most lightning consisted of updraft flashes, transporting charge vertically from the lower negative region up to the positive region at the top of the updraft. After about 15 min, when there was enough positive charge in regions 10 to 20 km from the updraft, we observed a transition where there were fewer updraft flashes and more extensive flashes which would start in the negative region of the updraft, follow the positive charge to the top of the updraft, and then follow the positive layer until reaching another concentration of positive charge 10 to 20 km away from the updraft.

[83] 2. In the updraft, the balance of forces due to wind, gravity, and drag on hydrometeors results in the positive charge being propelled much higher than the negative charge, leading to charge separation (see the updraft flash in Figure 18). The top of the updraft was positively charged and the bottom was negatively charged. In the strong southern updraft U1, positive particles reached an altitude of 14 km, while negative particles were located between 7 and 10 km in altitude. In the weaker northern updraft U2, the positive particles reached 11 km altitude, while the negative charge was located between 5 km and 8 km in altitude.

[84] 3. Outside the updraft, the positive and negative regions were separated by around 2 km vertically. Both the positive and negative charge decrease in altitude as we move away from an updraft. This separation of charge and decrease in altitude is seen in an average sense in Figures 31 (bottom) and Figure 32 (top), where we plot the mean altitude of charge as a function of distance north; this decrease is seen in the individual flashes such as Flash 2 in Figure 18 (extensive flash emanating from U1) and Flash 5 in Figure 20 (extensive flash emanating from U2); this decrease is seen in a cumulative sense in Figure 10 where we plot all the LMA pulses and their associated signs. In each case, the decay in altitude outside the updraft is at a rate between 1 km and 2 km in altitude per 10 km in horizontal distance. The mean altitude of the positive charge layer suggested by our study drops down to about 8 km when 15 km from U1, while the mean altitude of the inferred negative charge layer reaches 5.5 km when 15 km away from U1. It is possible that this drop represents the fall of charged hydrometeors under gravity or the effect of downdrafts which complete the U1 convective cell.

[85] 4. Let us use the letters P and N to denote sources for positive and negative charge, respectively. First, there is a P region at the top of each updraft. This region was revealed by the updraft flashes, such as Flashes 1 and 4. Although some positive charge at the top of the updraft was neutralized by lightning, a significant amount of positive charge was transported away from the updraft where it was neutralized by extensive flashes. Based on the flashes that we could analyze, we conjecture that a P region extends roughly along the yellow/orange portion of Figure 29 closest to the boundary of a semicircle centered near U1 with the axis of symmetry parallel to the direction of the wind. The N region is much easier to describe. The negative charge seems to occupy a cone with its peak centered in the updraft. The altitude of the top of the cone approaches 10 km in a strong updraft, while dropping to 6 km when 10 to 15 km away from the updraft. The linear cross section of the cone is seen in Figure 10 and in Figure 32 (top).

[86] 5. The negative charge drooping away from the updraft became the principal source of charge for cloud-to-ground flashes. Most CG flashes transported low negative charge at an altitude around 6 km to the ground. A few CG flashes transported higher negative charge near an updraft to the ground (the upper dashed peak in Figure 32 (bottom)). The IC flashes mostly transported more elevated negative charge (when compared to CG flashes) to the positive region (see the solid line in Figure 32 (bottom)).

[87] 6. Most of the charge transport in the thunderstorm was due to IC flashes. We estimate that nearly 6 times as much charge was transported by IC flashes when compared to CG flashes. The ratio of the average charge transport for an IC flash to the average charge transport for a CG flash was 1.6. The estimated average generator current associated with the combined updrafts during the period between 1950 UT and 2030 UT was 2.3 A.

[88] We now compare the charge structure deduced in our analysis to that found in other studies. Charge models for a thunderstorm have been proposed for many years. Dipole models were proposed by *Wilson* [1916, 1920, 1925] and *Simpson* [1909, 1927], which could be viewed as simplified models of the charge structure that we determined. Tripole models were later suggested by *Simpson and Scrase* [1937] and *Simpson and Robinson* [1941]. Electric field balloon soundings were made by *Marshall and Rust* [1991, 1993]; *Stolzenburg and Marshall* [1994]; *Stolzenburg et al.* [1994, 1998c, 1998a, 1998b, 2001, 2002] to estimate the charge density in a thundercloud. These sounding were made through mesoscale convective systems, isolated supercells, and isolated New Mexican mountain storms. The charge density estimates were obtained by a one-dimensional approximation to Gauss' law,

$$\rho = \epsilon \frac{\Delta E_z}{\Delta z}, \tag{8}$$

where ρ is charge density, ϵ is the permittivity of air, Δz is the change in vertical altitude of the balloon, and ΔE_z is the corresponding change in the vertical component of the electric field. We compare the charge structure indicated by our charge transport analysis to the balloon soundings given by *Stolzenburg et al.* [1998a, 1998b] for New Mexican mountain storms. One difference between our analysis and

the balloon soundings is that we only detect charge transported by lightning, while a balloon sounding detects all net charge. Hence, regions of charge in the thundercloud that are too small to cause lighting would not be seen in the charge transport analysis, which detects the principal charge regions, but these regions could be detected by the balloon sounding.

[89] The authors in the balloon sounding studies often partition their results into two sets corresponding to flights near the center of convection and flights outside the center of convection. The results shown in Figure 6 of *Stolzenburg et al.* [1998a] or Figure 1 of *Stolzenburg et al.* [1998b] for flights in or near the center of convection are quite similar to the two-layer charge structure observed in the charge transport analysis. One difference is that the balloon soundings detect a negative screening layer at the top of the thundercloud and a lower region of positive charge which is not seen in our analysis. On the other hand, the results shown in Figure 6 of *Stolzenburg et al.* [1998a] or Figure 2 of *Stolzenburg et al.* [1998b] for flights outside the center of convection are different; the authors report one or more additional charge layers not seen in our analysis. Possible explanations for the good agreement near the center of convection and the poor agreement outside the center of convection are the following.

[90] 1. The approximation (8) used to estimate charge density could be relatively good near the center of convection, and not as good away from the center of convection where the neglected partial derivatives in E_x and E_y with respect to x and y might effect the interpretation of the balloon sounding data.

[91] 2. Another possibility is that the additional charge layers are locally present. In Figure 10 the separation between positive and negative LMA pulses is rather clear near the updrafts, but midway between the updrafts, the separation is not as clear, and there is the potential for some mixing of layers from wind turbulence and interactions between the updrafts. A balloon flight through this mixed region could detect additional layers locally.

[92] 3. The storm of 18 August 2004 had a different structure from the storms analyzed by *Stolzenburg et al.* [1998a, 1998b].

[93] Clearly, further analysis and experimental work are needed to understand the connections between these studies.

[94] **Acknowledgments.** This work was funded primarily by grants 0619080, 0724750, 0724771, and 0331164 from the National Science Foundation. Additional funding was provided by the Office of the President of New Mexico Institute of Mining and Technology, by the Irving and Marion Langmuir bequest to Langmuir Laboratory, and by the National Aeronautics and Space Administration through the New Mexico Space Grant Consortium. The field operations at Langmuir Laboratory were conducted on the Cibola National Forest under a special use permit from the U.S. Forest Service. Harald Edens preprocessed the LMA data. The NEXRAD PPI scans for National Weather Service station KABX, Albuquerque, were obtained from the National Oceanic and Atmospheric Administration (NOAA) and their National Climatic Data Center (NCDC). The NEXRAD data were particularly useful for pinpointing the location of the thunderstorm updrafts and for determining the structure of the thunderstorm. The NEXRAD Level II data [*Crum et al.*, 1993], when combined with the NCDC Weather and Climate Toolkit, were especially helpful for visualizing the updraft in three dimensions. The radar imagery in Figure 8 was provided by Steve Ansari and Steve DelGreco at NCDC. Input received from William P. Winn during the drafting of this paper is gratefully acknowledged. Data from the National Lightning Detection Network (NLDN) were provided by Vaisala Inc.

References

Bruning, E. C., W. D. Rust, T. J. Schuur, D. R. MacGorman, P. R. Krehbiel, and W. Rison (2007), Electrical and polarimetric radar observations of a multicell storm in TELEX, *Mon. Weather Rev.*, *35*, 2525–2544.

Coleman, L. M., T. C. Marshall, M. Stolzenburg, T. Hamlin, P. R. Krehbiel, W. Rison, and R. J. Thomas (2003), Effects of charge and electromagnetic potential on lightning propagation, *J. Geophys. Res.*, *108*(D9), 4298, doi:10.1029/2002JD002718.

Crum, T. D., and R. L. Alberty (1993), The WSR-88D and the WSR-88D operational support facility, *Bull. Am. Meteorol. Soc.*, *74*, 1669–1687.

Crum, T. D., R. L. Alberty, and D. W. Burgess (1993), Recording, archiving, and using WSR-88D data, *Bull. Am. Meteorol. Soc.*, *74*, 645–653.

Crum, T. D., R. E. Saffle, and J. W. Wilson (1998), An update on the NEXRAD program and future WSR-88D support to operations, *Weather Forecasting*, *13*, 253–262.

Cummins, K. L., and M. J. Murphy (2009), An overview of lightning locating systems: History, techniques, and data uses, with an in-depth look at the U.S. NLDN, *IEEE Trans. Electromagn. Compat.*, *51*, 499–518.

Fleenor, S. A., C. J. Biagi, K. L. Cummins, E. P. Krider, and X.-M. Shao (2009), Characteristics of cloud-to-ground lightning in warm-season thunderstorms in the Central Great Plains, *Atmos. Res.*, *91*, 333–352.

Hager, W. W., J. S. Nisbet, J. R. Kasha, and W.-C. Shann (1989), Simulations of electric fields within a thunderstorm, *J. Atmos. Sci.*, *46*, 3542–3558.

Hager, W. W., R. G. Sonnenfeld, B. C. Aslan, G. Lu, W. P. Winn, and W. L. Boeck (2007), Analysis of charge transport during lightning using balloon borne electric field sensors and LMA, *J. Geophys. Res.*, *112*, D18204, doi:10.1029/2006JD008187.

Klazura, G. E., and D. A. Imy (1993), A description of the initial set of analysis products available form the NEXRAD WSR-88D system, *Bull. Am. Meteorol. Soc.*, *74*, 645–653.

Lhermitte, R., and P. R. Krehbiel (1979), Doppler radar and radio observations of thunderstorms, *IEEE Trans. Geosci. Electron.*, *17*, 162–171.

MacGorman, D. R., and W. D. Rust (1998), *The Electrical Nature of Thunderstorms*, 422 pp., Oxford Univ. Press, New York.

Marshall, T. C., and W. D. Rust (1991), Electric field soundings through thunderstorms, *J. Geophys. Res.*, *96*(D12), 22,297–22,306.

Marshall, T. C., and W. D. Rust (1993), Two types of vertical electrical structures in stratiform precipitation regions of mesoscale convective systems, *Bull. Am. Meteorol. Soc.*, *74*, 2159–2170.

Rakov, V. A., and M. A. Uman (2003), *Lightning Physics and Effects*, Cambridge Univ. Press, Cambridge, U. K.

Rison, W., R. J. Thomas, P. R. Krehbiel, T. Hamlin, and J. Harlin (1999), A GPS-based three-dimensional lightning mapping system: Initial observations in central New Mexico, *Geophys. Res. Lett.*, *26*(23), 3573–3576.

Rust, W. D., D. R. MacGorman, E. C. Bruning, S. A. Weiss, P. R. Krehbiel, R. J. Thomas, W. Rison, T. Hamlin, and J. Harlin (2005), Inverted-polarity electrical structures in thunderstorms in the Severe Thunderstorm Electrification and Precipitation Study, *J. Atmos. Sci.*, *76*, 247–271.

Scott, R., P. Krehbiel, M. Stanley, and S. McCrary (1995), Relation of lightning channels to storm structure from interferometer and dual-polarization radar observations, paper presented at 27th Conference on Radar Meteorology, Am. Meteorol. Soc., Vail, Colo.

Shao, X. M., and P. R. Krehbiel (1996), The spatial and temporal development of intracloud lightning, *J. Geophys. Res.*, *101*(D21), 26,641–26,668.

Simpson, G. C. (1909), On the electricity of rain and snow, *Proc. R. Soc., Ser. A*, *83*, 394–404.

Simpson, G. C. (1927), The mechanism of a thunderstorm, *Proc. R. Soc., Ser. A*, *114*, 376–401.

Simpson, G. C., and G. D. Robinson (1941), The distribution of electricity in thunderclouds, II, *Proc. R. Soc., Ser. A*, *177*, 281–329.

Simpson, G. C., and F. J. Scrase (1937), The distribution of electricity in thunderclouds, *Proc. R. Soc., Ser. A*, *161*, 309–352.

Sonnenfeld, R. G., J. Battles, G. Lu, and W. P. Winn (2006), Comparing E-field changes aloft to lightning mapping data, *J. Geophys. Res.*, *111*, D20209, doi:10.1029/2006JD007242.

Stolzenburg, M., and T. C. Marshall (1994), Testing models of thunderstorm charge distributions with Coulomb's law, *J. Geophys. Res.*, *99* (D12), 25,921–25,932.

Stolzenburg, M., T. C. Marshall, W. D. Rust, and B. F. Smull (1994), Horizontal distribution of electrical and meteorological conditions across the stratiform region of a mesoscale convective system, *Mon. Weather Rev.*, *122*, 1777–1797.

Stolzenburg, M., W. D. Rust, and T. C. Marshall (1998a), Electrical structure in thunderstorm convective regions: 2. Isolated storms, *J. Geophys. Res.*, *103*(D12), 14,079–14,096.

Stolzenburg, M., W. D. Rust, and T. C. Marshall (1998b), Electrical structure in thunderstorm convective regions: 3. Synthesis, *J. Geophys. Res.*, *103*(D12), 14,097–14,108.

Stolzenburg, M., W. D. Rust, B. F. Smull, and T. C. Marshall (1998c), Electrical structure in thunderstorm convective regions: 1. Mesoscale convective systems, *J. Geophys. Res.*, *103*(D12), 14,059–14,078.

Stolzenburg, M., T. C. Marshall, and W. D. Rust (2001), Serial soundings of electric field through a mesoscale convective system, *J. Geophys. Res.*, *106*(D12), 12,371–12,380.

Stolzenburg, M., T. C. Marshall, W. D. Rust, and D. L. Bartels (2002), Two simultaneous charge structures in thunderstorm convection, *J. Geophys. Res.*, *107*(D18), 4352, doi:10.1029/2001JD000904.

Taylor, W. L., E. A. Brandes, W. D. Rust, and D. R. MacGorman (1984), Lightning activity and severe storm structure, *Geophys. Res. Lett.*, *11*(5), 545–548.

Tessendorf, S. A., S. A. Rutledge, and K. C. Wiens (2007), Radar and lightning observations of normal and inverted polarity multicellular storms from STEPS, *Mon. Weather Rev.*, *135*, 3665–3681.

Thomas, R. J., P. R. Krehbiel, W. Rison, T. Hamlin, J. Harlin, and D. Shown (2001), Observations of VHF source powers radiated by lightning, *Geophys. Res. Lett.*, *28*(1), 143–146.

Thomas, R. J., P. R. Krehbiel, W. Rison, S. J. Hunyady, W. P. Winn, T. Hamlin, and J. Harlin (2004), Accuracy of the Lightning Mapping Array, *J. Geophys. Res.*, *109*, D14207, doi:10.1029/2004JD004549.

Vonnegut, B. (1983), Deductions concerning accumulations of electrified particles in thunderclouds based on electric field changes associated with lightning, *J. Geophys. Res.*, *88*(C6), 3911–3912.

Weiss, S. A., W. D. Rust, D. R. MacGorman, E. C. Bruning, and P. R. Krehbiel (2008), Evolving complex electrical structure of the STEPS 25 June 2000 multicell storm, *Mon. Weather Rev.*, *136*, 741–756.

Wiens, K. C., S. A. Rutledge, and S. A. Tessendorf (2005), The 29 June 2000 supercell observed during STEPS Part II: Lightning and charge structure, *J. Atmos. Sci.*, *62*, 4151–4177.

Wilson, C. T. R. (1916), On some determinations of the sign and magnitude of electric discharges in lightning flashes, *Proc. R. Soc., Ser. A*, *92*, 555–574.

Wilson, C. T. R. (1920), Investigations on lightning discharges and on the electric field of thunderstorms, *Philos. Trans. R. Soc. A*, *221*, 73–115.

Wilson, C. T. R. (1925), The electric field of a thundercloud and some of its effects, *Proc. R. Soc., Ser. D*, *37*, 32–37.

B. C. Aslan, Department of Mathematics and Statistics, University of North Florida, Jacksonville, FL 32224, USA.

J. D. Battles, Space Instrumentation and Systems Engineering, Los Alamos National Laboratory, Los Alamos, NM 87545, USA.

T. D. Crum, WSR-88D Radar Operations Center, NWS, NOAA, 1200 Westheimer Drive, Norman, OK 73069, USA.

W. W. Hager, Department of Mathematics, University of Florida, PO Box 118105, Gainesville, FL 32611, USA. (hager@ufl.edu)

M. T. Holborn and R. Ron, School of Architecture, University of Florida, Gainesville, FL 32611-5702, USA.

R. G. Sonnenfeld, Department of Physics, New Mexico Institute of Mining and Technology, Socorro, NM 87801, USA.